Exploration of Parameters Affecting Jet Injection Using a High-Speed X-ray Imaging System

by

Gee Hoon Park

Submitted to the Department of Mechanical Engineering
in partial fulfillment of the requirements for the degree of

Master of Science in Mechanical Engineering

at the

MASSACHUSETTS INSTITUTE OF TECHNOLOGY

June 2015

Author ..... Signature redacted
Department of Mechanical Engineering
May 21, 2015

Certified by ..... Signature redacted
Ian W. Hunter
Professor of Mechanical Engineering
Thesis Supervisor

Accepted by ..... Signature redacted
David E. Hardt
Chairman, Department Committee on Graduate Students

Exploration of Parameters Affecting Jet Injection Using a High-Speed X-ray Imaging System

by

Gee Hoon Park

Submitted to the Department of Mechanical Engineering
on May 21, 2015, in partial fulfillment of the
requirements for the degree of
Master of Science in Mechanical Engineering

Abstract

This thesis explores the effects of two parameters, contact force and jet shape, on jet injection using a high-speed X-ray imaging system. The scope of the thesis is twofold. The first part describes the process of optimization of the high-speed imaging system for better stress distribution and deformation of the porcine tissue block used in the jet injection experiment. The parameters for the high-speed X-ray imaging system, namely the voltage and the current of the X-ray source and the exposure time of the high-speed camera, were optimized for tissue blocks with different width by evaluating the signal to noise ratio (SNR) of X-ray images. High-speed X-ray images of jet injection into tissue with dimension of 80 mm $\times$ 65 mm (L$\times$W) $\times$ 40 mm (H) suggested that the image quality of the current system was susceptible to varying X-ray absorptions associated dependent on the width of the imaged tissue. As an alternative solution, a jet injection experiment on a porcine tissue with asymmetric dimension of 80 mm $\times$ 30 mm (L$\times$W) $\times$ 30 mm (H) was conducted. Based on the results from the experiment, it was concluded that asymmetric dimension will improve the stress distribution and the deformation of tissue of porcine tissue in jet injection, with reasonable image quality while possibly introducing a defect of an asymmetric dispersion pattern. The second part of this thesis examines the effects of contact force and jet shape on the jet injection using the newly optimized parameters for the imaging system. The presence of 1 N contact force in jet injection reduced the required jet pressure to breach the tissue by at most 8 MPa as the contact force pre-tensioned the tissue surface. Also the dispersion patterns jet injections with presence and absence of the contact force showed that the pre-tensioning can possibly improve the delivery of injectate into the tissue. In addition, jet injections into tissue analog and *ex vivo* porcine tissue suggested that jet injection with a collimated jet shape can result in a deeper penetration than that with a dispersed jet shape.

Thesis Supervisor: Ian W. Hunter
Title: Professor of Mechanical Engineering

Acknowledgments

First, I would like to express the deepest appreciation to my advisor Professor Ian Hunter for letting me fulfill my dream of being a student here at MIT and giving this opportunity to research in his lab. All the inspirations and knowledge I've gotten from him has been developing me as a true engineer.

I would like to extend my sincere gratitude to Dr. Cathy Hogan for all her dedications and supports. Dr. Hogan continually guided me to the next step of my research and mentored me with key insights.

I would also like to thank Ms. Kate Melvin for giving me a happy smile whenever I see her.

Bioinstrumention Lab member. Thank you to Ashin Modak for giving me tremendous advices, ideas and help, to John Liu for giving me so much sincere support, to Nick Demas, Ashley Brown, Craig Cheney, Seyed Mirvakili and Anshul Singhal for being good friends to me.

Thank you to Minkyun, who brought me into MIT and supported me whenever I needed a help.

To my parents and brother, I know we are always loving each other wherever we are.

Lastly, to my love, Eunjee. I'll always be living for the love of you.

THIS PAGE INTENTIONALLY LEFT BLANK

Contents

List of Figures

THIS PAGE INTENTIONALLY LEFT BLANK

Chapter 1

Introduction

Several problems are associated with the use of conventional needle-based drug delivery system, which include needle stick injuries, sharp disposals and psychological trauma caused by a belonephobia. An estimated 400,000 needle stick injuries and other sharps-related injuries are sustained by hospital-based health-care personnel in the US [1]. Needle-related accidents are especially problematic in developing countries because injection safety is a notorious problem: improper practices involving non-sterile needles and syringes, often reused from one person to another, cause abscesses and transmit blood-borne pathogens, such as hepatitis B and C and HIV [2]. Thus, acceptability and compliance of immunization in developing countries can be increased if the vaccination can be conducted without needles [3].

Needle-free jet injection is a promising solution to the problems of the conventional needle-based drug delivery. While work has been done to evaluate the mechanics of jet injection, more knowledge on jet injection dynamics needs to be attained to better understand jet injection and the parameters that determine dispersion pattern in the tissue.

This thesis explores the parameters affecting jet injection powered by a Lorentz-force needle-free jet injector using a high-speed X-ray imaging system. Chapter 2 provides background on the needle-free jet injection, its mechanism and X-ray imaging. Chapter 3 describes the optimization process of the high-speed X-ray imaging system for jet injection into a large tissue block. Chapter 4 explores the effect of

contact force on the critical stress of the porcine tissue. Chapter 5 investigates the effect of jet shape on jet dispersion. Finally, Chapter 6 gives a brief summary of this thesis and future work.

Chapter 2

Background

2.1 Needle Free Jet Injection

Needle-free jet injection is an innovative way to deliver a variety of medicines into a patient's body without using a traditional needle. It was first introduced by Hingson and Hughes [4] as an alternative method for traditional needle-based drug delivery. The key concept of needle free jet injection is the generation of a high pressure fluid jet to penetrate the skin and deliver the drug into the skin through the stratum corneum and into the underlying tissue as described in Fig. 2.2. Commercial needle-free jet injectors have been powered by a variety of sources to propel the drug at high velocity through a tiny orifice, which include compressed springs [5] [6], compressed gases [7], or explosive chemicals [8] as shown in Fig. 2-2. They are used to deliver several different types of drugs such as vaccines, proteins [9] small molecules(e.g. steroids, antibiotics), and other macromolecules including DNA-based therapeutics [10]. Depending on the target layer of the drug delivered some current devices are designed to adjust the power of the jet fluid [5] [7].

There are many advantages associated with the needle free injection technology. The speed of delivery when compared to delivery using a needle and syringe, removal of psychological (e.g. fear of needles) and physical (e.g. neuropathic) barriers, and the potential to reduce the frequency of injections can lead to increased acceptance and compliance. The use of these devices will also eliminate the costs associated with

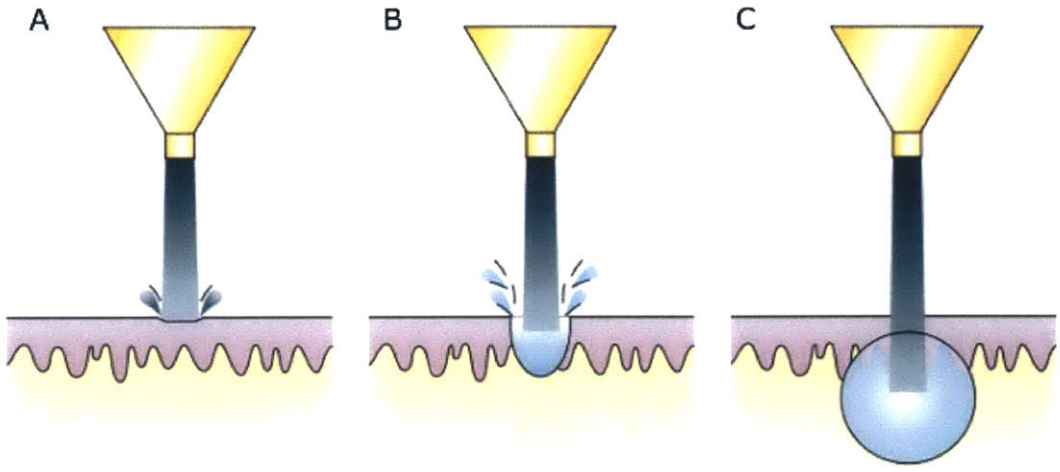

Figure 2-1: A jet injection mechanism model. (A) A high speed jet impinges on the skin, and (B) depending on the power of a jet, breaches the skin, creating opening. (C) A bolus of liquid drug is created and a liquid is delivered. Figure adapted from [11].

needle stick injuries and sharps disposal. In addition, several studies have showed that vaccine delivery using needle free jet injection can elicit a better immune response than observed following delivery using a conventional needle syringe [12] [13] [14]. Despite these advantages, needle-free jet injectors have been slow to replace conventional needle-based drug delivery. Some of this hesitation may be due to the association of early multi-use jet injectors with cross contamination [15] and skin lacerations and bruising [16] [17]. The introduction of disposable single use cartridges together with improved control over delivery parameters has resulted in a resurgence of interest in jet injection technology as evidenced by the number of jet injection systems currently being marketed.

2.2 Jet Injection Mechanism

The mechanism of jet injection into skin has been described as two consecutive events, skin fracture followed by fluid dispersion [18]. Comley and Shergold showed that jet penetration of a soft solid and adipose tissue is done by forming and opening a planar

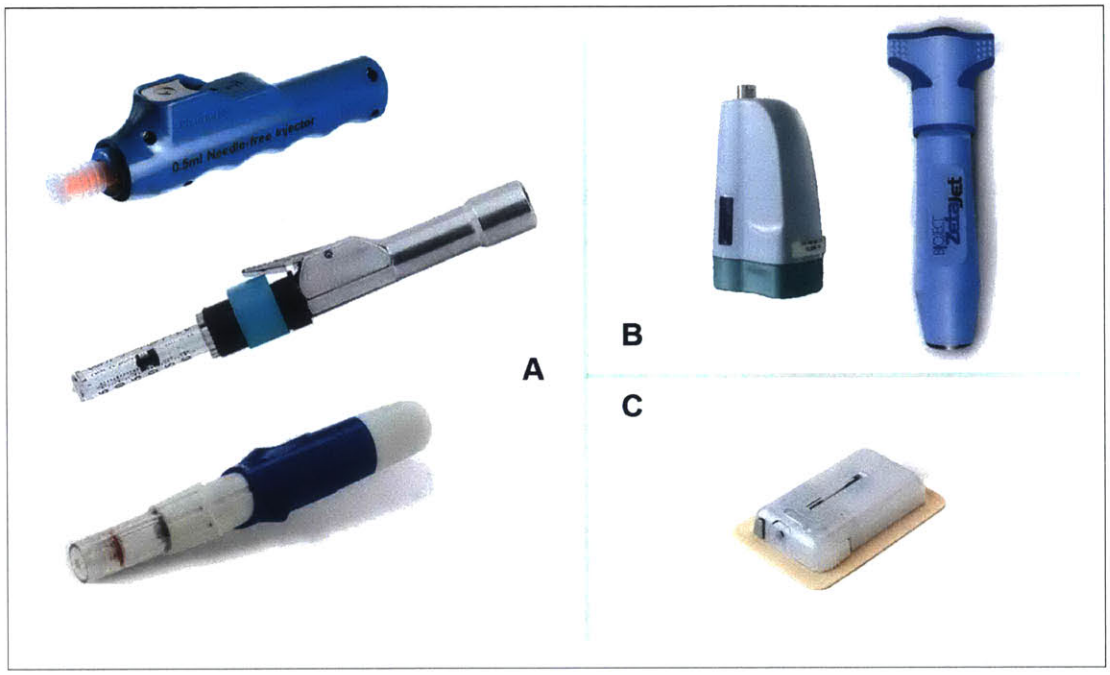

Figure 2-2: Various types of needle-free jet injectors: (A) injectors driven by springs [6] [5], (B) injectors driven by compressed gas [7], and (C) an injector driven by explosive reactions [8].

crack, which is similar to the behavior of a sharp-tipped punch [19] [20]. As illustrated in Fig.2-3, the crack face is opened as a wedge shape and closed after the punch is removed.

Several papers explored important parameters that affect the jet injection mechanism. Schramm-Baxter and Mitragotri demonstrated that jet penetration and dispersion were dependent on jet velocity and nozzle geometry [18], which were incorporated into jet power in a later paper [21]. They demonstrated that as the power at the nozzle exit increased, the hole depth created by the jet increased as shown in Fig. 2-4A. In addition, they showed that the properties of the skin affected drug delivery by jet injection. As the Young's modulus of the skin increased, both the hole depth and fluid delivered to the tissue were found to decrease as shown in Fig. 2-4B [22].

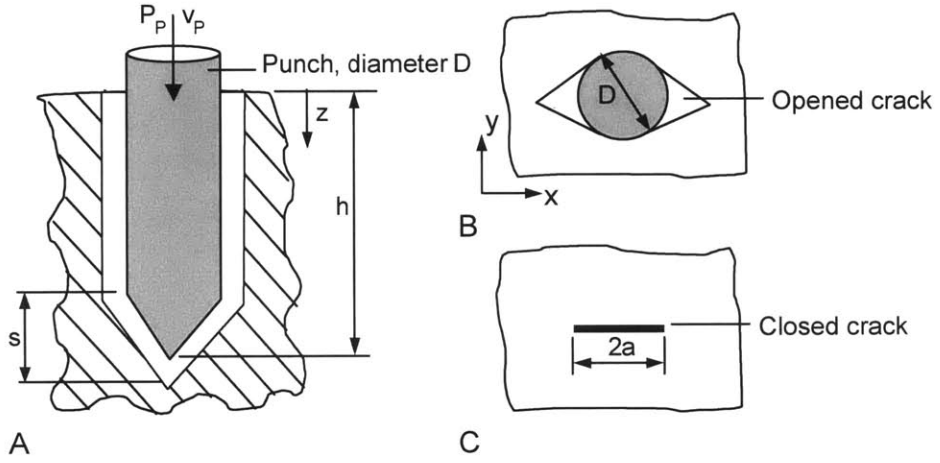

Figure 2-3: Liquid jets and sharp-tipped punches penetrate a hole in a tissue by forming a planar crack, as illustrated in (A) and (B). The planar crack closes after the removal of the punch (C). Figure adapted from [20].

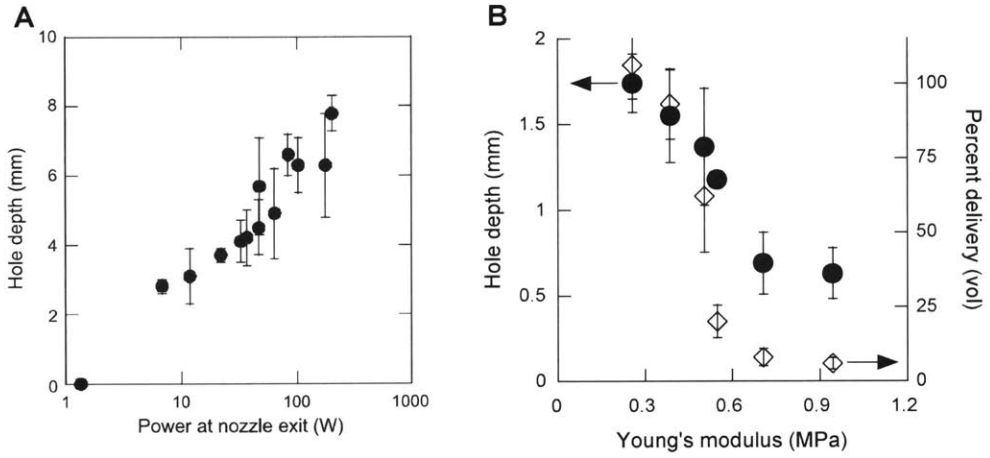

Figure 2-4: (A) Experimental data showing that the hole depth created by the jet has a positive relation with the jet power at nozzle exit. Note that the jet power axis is logarithmic. (B) The hole depth decreased as the Young's modulus of the skin increased. Figure adapted from [21] [22].

2.3 Lorentz-Force Jet Injector

The MIT BioInstrumentation Lab has developed a Lorentz-force powered jet injection device that allows for real-time control of the pressure profile [23] [24] [25] [26]. The profile can be described by three parameters; a brief high-speed phase (v_{jet}) during which the jet penetrates the tissue to the desired depth, a time length (t_{jet}) of v_{jet} and a second low-speed phase (v_{ft}) during which the majority of the fluid is delivered (Fig. 2-6). The device consists of a custom-made Lorentz-force motor, custom-built housing, a linear potentiometer (688-RDC10320RB, Mouser Electronics) [27] as a position sensor and a commercially available drug ampoule (Injex ampoule, Injex Pharma Ltd.) [5]. The Lorentz-force motor was wound with 0.32 mm diameter (28 gauge wire), and had a resistance of 12.25 Ω and an inductance of 8.07 mH [28]. The Bl force constant to the motor measured in a vertical configuration was 11.8 N/A for downward movement [28].

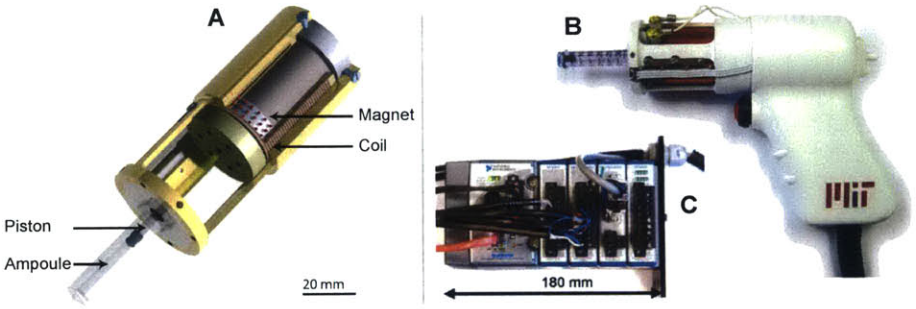

Figure 2-5: (A) Cutaway of Lorentz-force motor with ampoule attached. (B) A handheld version of Lorentz-force needle free jet injector and (C) compactRIO system for control. Images adapted from [26].

High-speed position monitoring and control is achieved in real-time using a National Instruments Compact RIO system [29] comprising a real-time controller (cRIO-9004, National Instruments) embedded in a reconfigurable field-programmable gate-array chassis (cRIO-9104) [30]. The software running in the Compact RIO system is written in National Instruments LabVIEW 2013. It consists of a real-time "host" application and FPGA "target" application in which user commands are interpreted

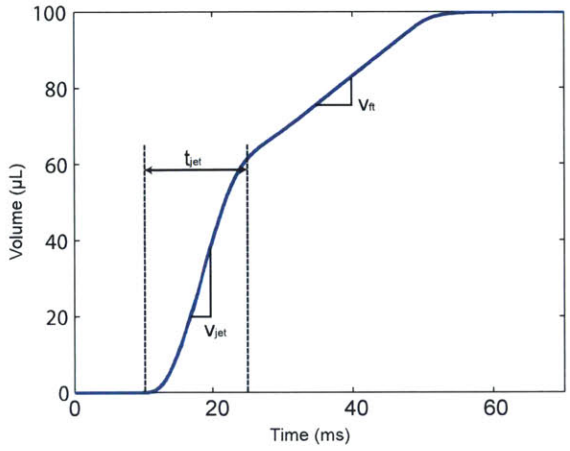

Figure 2-6: A typical position profile of a coil used in jet injection.

to generate desired velocity waveforms. Control of coil position was achieved using a proportional-integral-derivative (PID) controller.

The device provides advantages over other commercially available needle-free injectors since a fully controllable electromechnical actuator is able to create optimized pressure profiles for different volume delivery under a closed-loop control. A hardware part of Lorentz-force powered jet injector is shown in Fig. 2-5.

It has been found by several studies in our lab [30] [26] that penetration depth and dispersion pattern of jet injection using the Lorentz-force actuated needle free jet injector are characterized by the velocity profile of the jet. In particular, injections into tissue analogue and ex vivo mammalian tissue suggests that injection depth is related to the v_{jet} as it changes a brief high speed phase to breach the tissue. After the jet reaches to the target layer it starts delivering the fluid with a following jet velocity, v_{ft} [30].

2.4 Tissue Layers

By varying the input parameters defining the velocity waveform, we can vary the tissue layer targeted by actuation of the voice coil. To understand jet dispersion pattern, it is necessary to understand the structure of Tissue. Human skin repre-

sents the largest organ of the body (1.8 m^2 or 16% total body weight). It consists of the epidermis and dermis. The epidermis varies in thickness and composition dependent on location. While it is primarily made up of keratinocytes (95%), it also contains melanocytes, Langerhans cells, Merkel cells, and inflammatory cells. It consists of 5 layers, the stratum corneum, stratum lucidum, stratum granulosum, stratum spinosum, and stratum basale (or germinativum). The stratum lucidum is visible only in the palms and soles. The primary function of the epidermis is as a barrier to protect the body against pathogens, damage due to UV light, and chemical and mechanical stress.

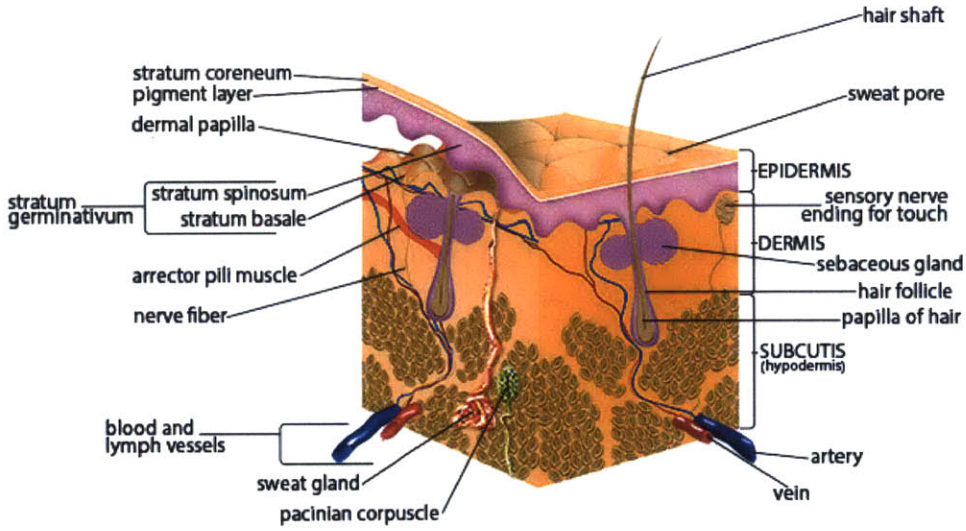

Figure 2-7: The structure of tissue is layered and consists of the epidermis, the dermis, the subcutaneous fat. Figure adapted from [31].

The dermis consists of a dense network of collagen fibers, elastin, glycosaminoglycans and proteoglycan core proteins. It is divided into two layers, a thin papillary layer and thicker reticular layer, and each contains sweat glands, hair roots, nerve cells and fibers, blood and lymph vessels. The dermis mainly provides nourishment and mechanical support to the epidermis. The components comprising this layer and their interactions are primarily responsible for the viscoelastic properties of the skin [32].

The layer beneath the dermis is called the hypodermis or subcutaneous fat layer. It contains mostly subcutaneous adipose tissue which forms adipocyte cells but also contains blood vessels, lymphatics, nerves and loose connective tissue. The hypodermis acts as an insulator for regulating the body temperature as well as a cushion to protect inner organ and bones.

The muscle lies underneath the subcutaneous fat layer. An individual muscle consists of hundreds or thousands of muscle fibers bundled together and wrapped in connective tissue. Each muscle fiber is surrounded by a connective tissue called endomysium, and fascia, connective tissue outside the endomysium, surrounds bundles of muscles. Each bundle of muscle fiber is surrounded by the perimysium, another type of connective tissue.

2.5 High speed X-ray Imaging System

In order to better understand the effect of jet parameters on jet injection into tissue, real time imaging was desired. This was achieved by injecting a high contrast agent into the tissue and visualizing the injection using a high-speed X-ray imaging system [28].

2.5.1 X-ray Imaging

X-ray imaging is a method of imaging an object using the different X-ray absorption rates of different objects. The medical application of X-ray imaging, called radiography, utilizes the ability of X-rays to penetrate the soft parts of human body. A detector, which consist of emulsion-gelatin containing radiation sensitive silver halide crystals and a blue-tinted base, is placed behind the object to capture the X-rays which pass through the object.

X-rays are generated at the X-ray source by colliding electrons emitted from a cathode to an anode. The cathode and the anode targets are placed inside the vacuum tube of the X-ray source (see Fig. 2-8). One important parameter of the X-ray source is the power of the X-ray tube. The power of the X-ray tube is calculated from the

peak voltage (source voltage) and the current (source current) between the cathode and anode.

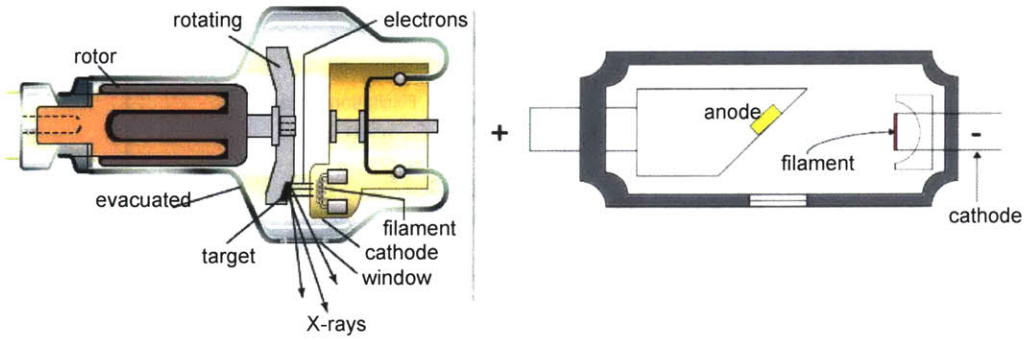

Figure 2-8: Diagram of a rotating X-ray tube. Electrons emitted from the cathode are accelerated toward the anode, then collide onto the anode material, generating X-rays. Figure adapted from [33].

The source voltage determines the kinetic energy of the X-ray as shown in Fig. 2-9. When the electrons strike the anode they lose energy by both collisional and radiative transfer; as a consequence heat, characteristic X-rays, and bremsstrahlung X-rays are produced. The bremsstrahlung spectrum, sometimes called the continuous spectrum, has its highest energy equal to the anode-to-cathode potential. Characteristic X-rays can be generated only if the incident electrons have sufficient energy to eject the K-shell electrons of the anode. Therefore, the energy of characteristic X-rays depends on the anode material of the X-ray source. The source current determines the density of X-ray beams by changing the number of photons generated from the anode.

Another important parameter is the focal spot size of the tube, which is the diameter of the anode where the electrons collide. The focal spot size determines the geometric unsharpness of the X-ray image [35]. The geometric unsharpness can be explained by the length of penumbra in Fig. 2-8.A penumbra is the shade of an object caused by lights coming from each edge of light source. The length of penumbra can

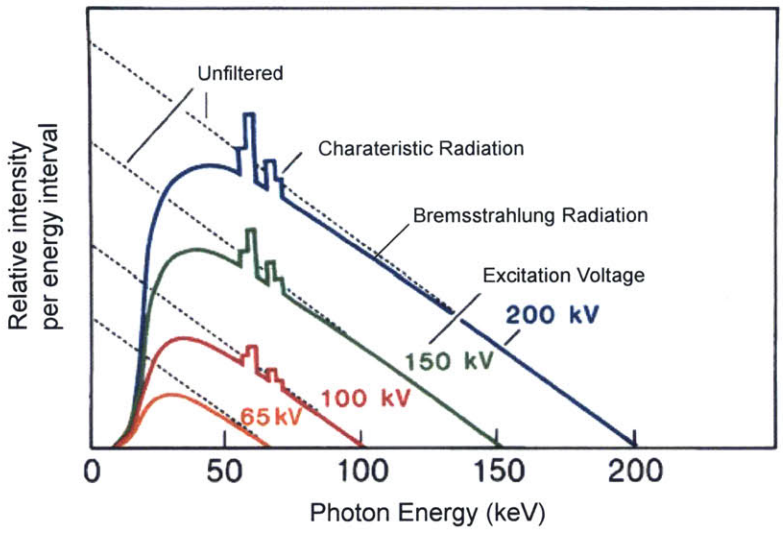

Figure 2-9: Spectrum of the X-rays emitted by an X-ray tube with a tungsten target, operated at different source voltages. The smooth, continuous curve is due to bremsstrahlung, and the spikes are characteristic K lines for tungsten atoms. Figure from [34].

be calculated from the equation below,

$$U_g = f \times \left(\frac{b}{a}\right), \tag{2.1}$$

where U_g is the length of a penumbra, f is the focal spot size, a is the distance from the source to the front surface of the object, and b is the distance between the object and the detector (see Fig.2-12). Therefore, a small focal spot size tends to have a sharper images. However, it also means that the electron stream that exits the cathode are more focused, which will cause excessive heat generation.

2.5.2 High-Speed X-ray Imaging System

The limitation of previous studies exploring the mechanism of jet injection was that they were based on valuating samples after injection [18] [22]. Information about the jet dispersion patterns or tissue damage gained from post injection results are not sufficient to explain the mechanism of jet injection. While studies were conducted

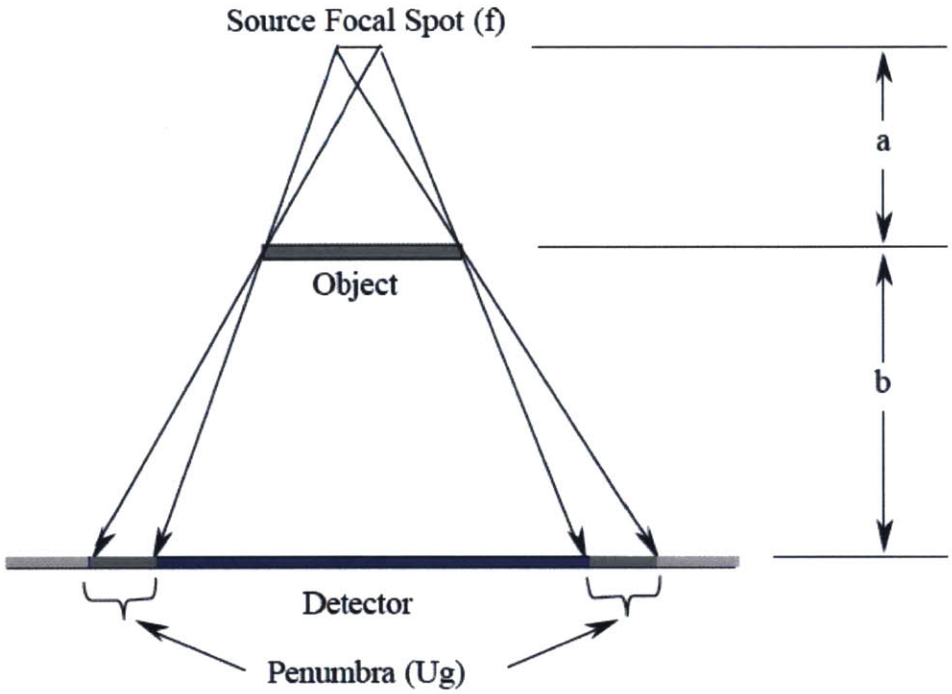

Figure 2-10: Geometric unsharpness, defined by the size of the penumbra Ug, is dependent on the X-ray source focal-spot size, the distance from the X-ray source to the front surface of the object, and the distance from the object to the detector. Figure from [35].

using high speed imaging of the tissue analogs [36] [30], the information obtained from these studies is limited with respect to its application to our understanding of the dynamics of injection into tissue. To better understand the mechanism of jet injection, a high-speed X-ray imaging system was assembled and jet injection of tissue using a high-contrast agent was imaged in real time (Fig. 2-11) [28].

The system consists of a high-speed digital camera (Phantom v9.0) , imaging intensifier, X-ray scintillator plate and X-ray source. The high-speed imaging camera is able to capture 1,000 fps at full resolution (1632 $\times$ 1200 pixels) and can capture up to 150,000 fps at reduced resolution (96 $\times$ 8 pixels). A thallium-doped cesium iodide (CsI(TI) scintillator plate (Hamamatsu, J6671-01) [37] is mechanically coupled with an image intensifier (Photek Limited, part number MCP125/F/S20/P46/GL) [38] so

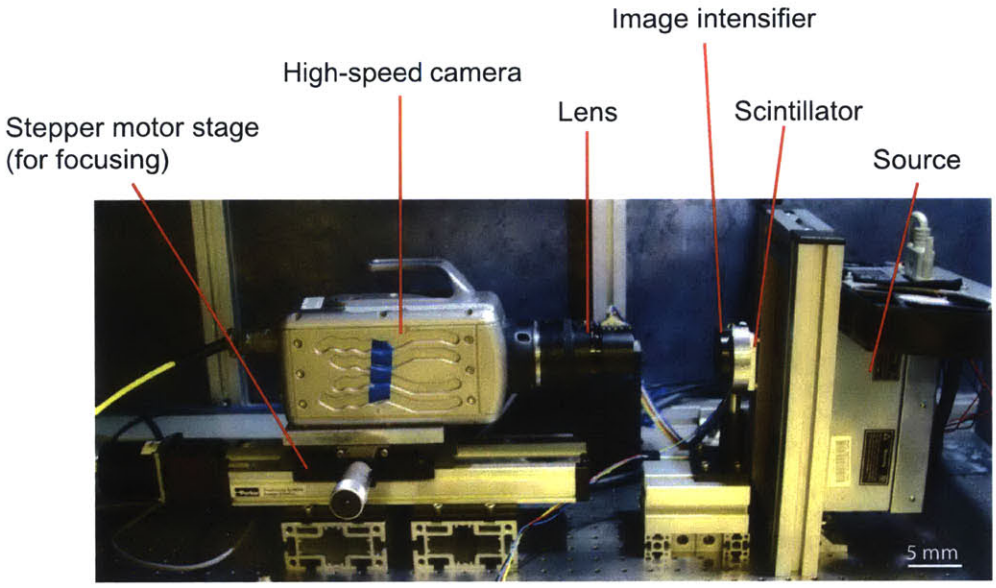

Figure 2-11: High-speed X-ray imaging system developed by Dr. Jean Chang in Bioinstrumentation Lab. Figure adapted from [28].

that visible light converted from the scintillator can be amplified and captured by the camera. The X-ray source (Source-Ray Inc., SB-80-500) is capable of outputting a maximum of 80 kVp with a current of 500 μA. This high-speed X-ray imaging system was used to image the jet injection of radiopaque dye (Nanoprobes, AuroVistTM 15nm) into ex vivo porcine abdominal tissue to investigate jet dispersion using a variety of delivery parameters [28].

Chapter 3

Optimization of a High-speed X-ray Imaging System for Needle Free Jet Injection

3.1 Motivation

Porcine abdominal skin is often considered to be a reliable analog for human skin based on morphological and functional data [39]. The Bioinstrumentation Lab uses ex vivo porcine abdominal skin with underlying subcutaneous tissue and muscle to evaluate injection of various agents including drugs using the Lorentz-force needle-free jet injector. In earlier X-ray imaging studies, tissue was cut to fit into clear plastic containers 22 mm × 22 mm (L×W) × 18 mm (H) in size [30].

One important issue caused by using such size of tissue is the inability to simulate the stress distribution and the deformation of the tissue similar to that experienced when injecting into a patient. Fig. 3-1 shows deformations of porcine tissue surfaces as a function of using differently sized tissue. The deformation of tissue when a needle-free ampoule is placed against it with comparable displacement is shown for tissue with dimensions of 22 mm × 22 mm (L×W) × 18 mm (H) 3-2A and 80 mm × 65 mm (L×W) × 40 mm (H) 3-1B. When the ampoule was pressed down on

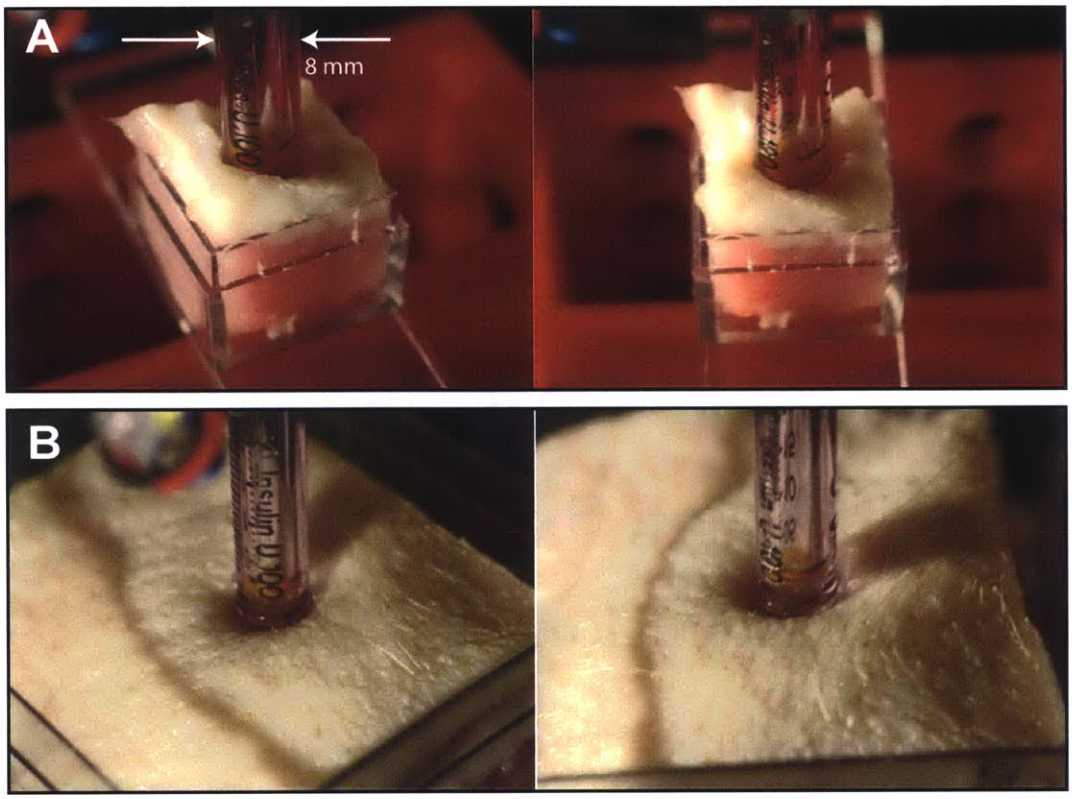

Figure 3-1: Images showing the tissue deformations of 22 mm × 22 mm (L×W) × 18 mm (H) size tissue (A) and 80 mm × 65 mm (L×W) × 40 mm (H) size tissue (B), when the ampoule applied pre-load.

both surfaces with the same displacement, the surface of the smaller block deformed more dramatically than that of the larger tissue block. This phenomenon is pictorially explained in the diagram in Fig. 3-2. In a large tissue block, the surface compressed by the ampoule transfers forces to the other surrounding tissues; the stress is distributed to more tissue in the larger block than in the smaller tissue block. Therefore, in a small tissue block, the stress on the surface of the tissue is expected to decay more rapidly towards the edge of the block. The stress distribution of the tissue which can be represented by the deformation of the tissue can have an influence on the jet injection mechanism. First of all, the stress distribution of the surface can determine the critical stress of the tissue thereby the jet power required to breach the surface can be changed. In addition, the deformation of the tissue changes the porosity of

the tissue, which results in changes in permeability of the tissue [28]. The difference in permeability will affect the jet dispersion pattern as the it determines how well the fluid can pass through the tissue.

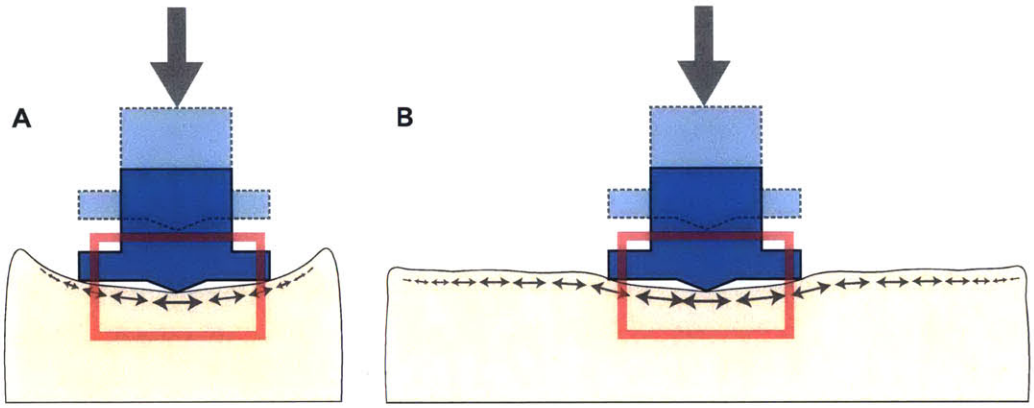

Figure 3-2: Diagram describing the boundary condition of the tissue surface with different sizes when the preload is present. (A) A small tissue block shows larger deformation and a rapid decay of stress distribution towards the edge of the tissue than a larger block (B).

Another issue is that the height of a container can limit the number or depth of the tissue layers that can be used for an injection thereby limiting studies designed to evaluate depth of penetration. Fig. 3-3 shows examples of porcine tissue blocks in containers of different width, depth, and height; any one of the parameters can restrict the scope of a study. Therefore, the size of the tissue block used in tissue injection experiments needs to be large enough to provide reasonable stress distribution and deformation of the tissue and thereby become a more realistic analog for the human skin.

However, one limitation of the high-speed X-ray imaging is that the image quality is determined by the width of the skin block in the X-ray beam direction. As the width increases, the intensity of X-ray at the scintillator plate decreases. The intensity of X-ray beam is defined as,

$$I = E \times \frac{N}{A \times \Delta t}, \tag{3.1}$$

where, E is the energy of a photon, N is the number of photons in a beam, A is

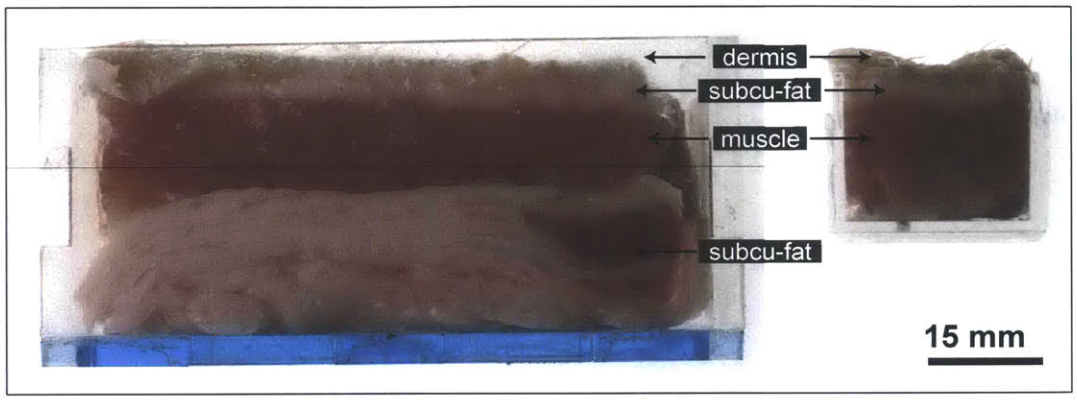

Figure 3-3: A comparison of tissues with different height. A large block (left) has more layers than the small block (right).

a cross section area of the beam and t is the time interval of the X-ray beam burst. Intensity has units of energy per unit area per unit time. The effect of tissue width on the intensity of the X-ray beam which arrives at the scintillator plate can be described by the Fundamental Photon Attenuation Law for a monoenergetic X-ray beam,

$$N = N_0 e^{-\mu \Delta x}, \tag{3.2}$$

where μ is the linear attenuation coefficient of the imaging object, x is the width of the object in an X-ray beam direction and N_0 is the number of phontons at $x = 0$ (see Fig. 3-4). By substituting (3.1) into (3.2), this law can also be written in terms of intensity as

$$I = I_0 e^{-\mu \Delta x}, \tag{3.3}$$

where I_0 is the intensity of the incident beam. Therefore, the intensity of the X-ray beam decreases exponentially as the width of the imaging object increases.

The intensity of the X-ray beam is an important factor in high speed X-ray imaging system as it will lead to a low quality X-ray image if the width of the tissue increases, which makes difficult to analyze the image. Given the opposing factors of realism and imaging, an optimization of the high-speed x-ray imaging system for experiment using large block of tissue is necessary, which is presented in this chapter.

To solve this problem, this chapter explores the optimization of the high-speed X-ray imaging system for experiment using large block of tissue.

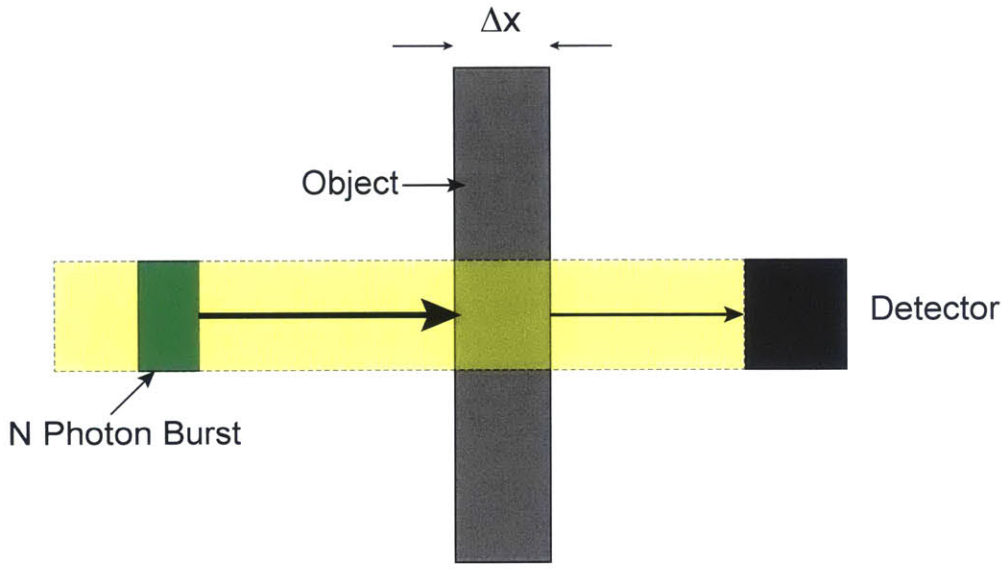

Figure 3-4: Diagram for X-ray beam penetration, absorption and detection. N photons pass through the object with the width of Δx with attenuation and arrive at the detector.

3.2 Considerations in Optimizing high-Speed X-ray Imaging System

Since the light output from the image intensifier was too low to be detected by the Phantom v9.0 at exposure times less than 490 μs, the maximum frame rate of the system was determined as 2000 fps in the previous high-speed X-ray imaging system for the imaging of a small porcine tissue block (22 mm width) [28]. The voltage and the current of the X-ray source used in the previous system were 40 kilovoltage peak (kVp) and 500 mA, and the image intensifier used full gain of 3,000 W/W at 550 nm wavelength.

When the width of a tissue sample increases, its corresponding X-ray image tends to have a lower image quality due to the decreasing intensity of the beam. In radio-

graphy, the image quality of an X-ray image can be evaluated by the local contrast, noise and signal to noise ratio (SNR). If the source is infinitesimal and there is no magnification in the imaging system, a rectangular object will cast a rectangular shadow on the detector with dimensions equal to the object's dimensions. Intensities on the detector will look like a rectangular function as shown in Fig. 3-5.

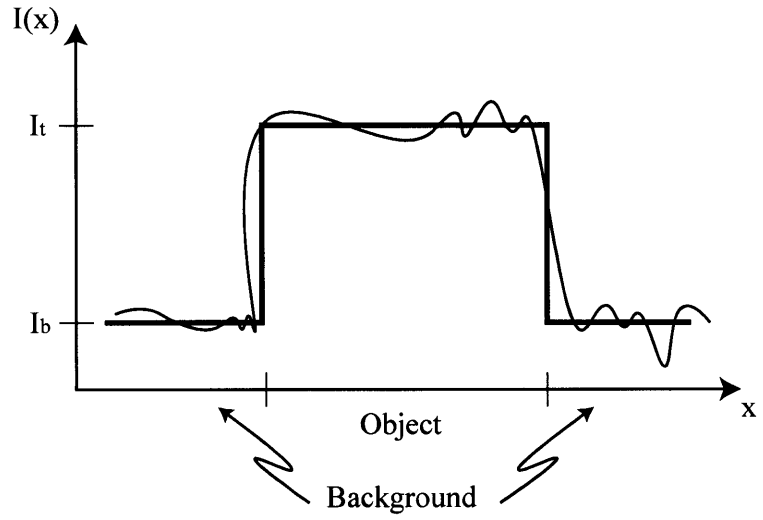

Figure 3-5: Detector intensities from a rectangular object.

The local contrast of the object, which indicates how well the object can be distinguished from the background, is given by

$$C = \frac{I_t - I_b}{I_b}, \tag{3.4}$$

where I_b is the background intensity and I_t is the object intensity on the detector plane. The noise is caused by quantum-related fluctuations in the backgournd [40], which can be characterized by a standard deviation σ_b,

$$\sigma_b = \sqrt{N_b}\left(\frac{E}{A\Delta t}\right), \tag{3.5}$$

where N_b is the number of photons which pass through the background and arrives at the detector. SNR can be used to quantify the effect of noise on image formation

by calculating the ratio between two parameters,

$$SNR = \frac{I_t - I_b}{\sigma_b} = \frac{CI_b}{\sigma_b}. \tag{3.6}$$

From (3.1), (3.4), (3.5) and (3.6), the SNR is given by,

$$SNR = C\sqrt{N_b}. \tag{3.7}$$

Therefore, to increase the SNR, either C or N_b must be increased. The local contrast of an X-ray image can be improved by changing the energy of the X-rays which is determined by the source voltage. However, increasing the source voltage will cause a trade-off in X-ray imaging, because changing the source voltage affects both the contrast and N_b. The contrast can be improved by decreasing the source voltage because the difference between the attenuation of different body tissues increases as energy decreases (see Fig. 3-6). However, as the energy of the photons decrease, fewer X-ray photons penetrate the body, resulting in a decrease in N_b. In a very low source voltage, the SNR is low. On the other hand, with increasing source voltage, even though the number of photons in a background increases, the contrast decreases as the attenuation coefficients for different types of body tissues become similar (see Fig. 3-6). This can also result in low SNR at very high source voltage. Therefore, depending on the object, the source voltage needs to be optimized to obtain reasonably good contrast with high enough SNR.

The number of photons might be increased by using a higher source current, increasing the duration of the X-ray pulse, or increasing the energy of the X-ray which would cause the beams to penetrate the body more deeply and therefore more photons would reach the detector. However, the source current values used in the system are the maximum of the device. A possible solution is to increase the exposure time of the high-speed camera which will have a simillar effect as increasing the duration of the X-ray pulse. One drawback of increasing the exposure time in the high-speed X-ray imaging system is that it will decrease the time resolution of the video which means less information will be obtained. A typical jet injection profile (Fig. 2-6) shows that

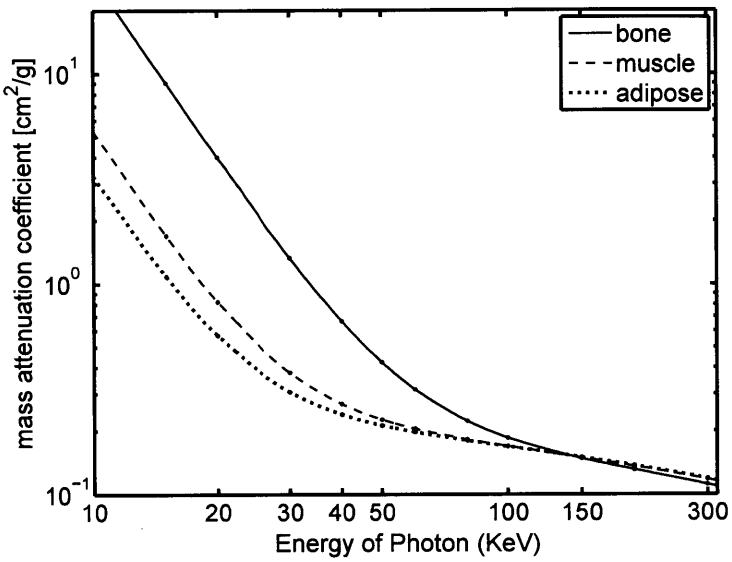

Figure 3-6: Mass attenuation coefficients for different body parts. Figure was reproduced from [41].

the injection finishes the 60 ms. In addition, from the previous X-ray imaging of jet injection [28], it was found that the breaching of the surface happens within 5 to 6 ms, which means increasing the exposure time from 500 μs to 1 ms will change the number of images that captures breaching within the 6 ms window from 12 to 6 ms. This decrease in images has a huge influence on analyzing the jet injection mechanism in real time. Therefore, the effect of the exposure time also needs to be explored to obtain the optimized image quality with enough information in it.

The summary of the optimization process is described in Fig. 3-7.

3.3 Optimizing Experimental Setup for Large Tissue Injection

The following sections explore the effect of the exposure time of the high-speed camera and the X-ray source voltage on X-ray image quality.

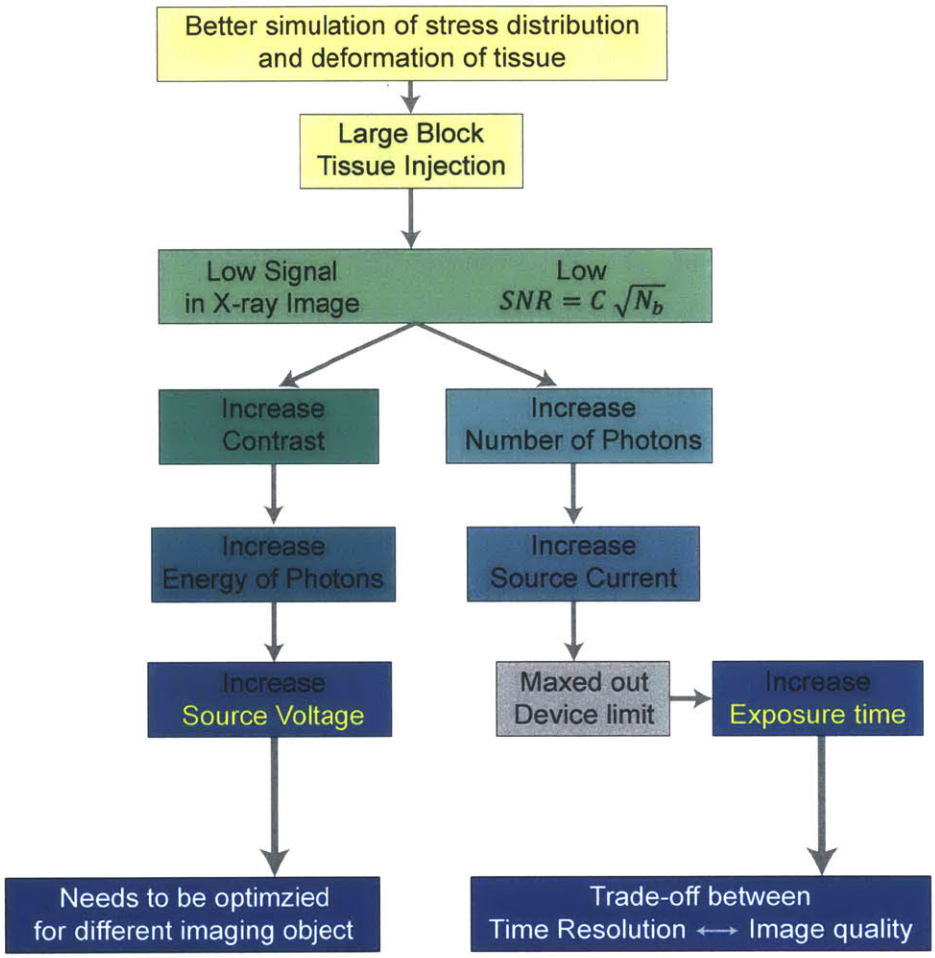

Figure 3-7: Summary of optimization of a high-speed X-ray imaging system for large tissue injection.

3.3.1 Experimental Methods

Post-mortem porcine tissue was obtained through the MIT Tissue Harvest Program using procedures approved by the MIT Committee on Animal Care and in accordance with the NIH Guide for the Use and Care of Laboratory Animals. Tissue was harvested from the abdomen of Yorkshire pigs approximately six months in age immediately after euthanasia and included muscle, subcutaneous fat, dermis, and epidermis. The samples were vacuum-sealed and stored at -80°C. Prior to experimentation, the samples were thawed to room temperature and cut into several blocks of 80 mm × 16 mm ($L \times W_t$) × 30 mm (H). The block was placed into the clear plastic 80 mm × 65 mm ($L \times W_c$) × 30 mm (H) container. By adding more blocks inside the container, the width of the tissue to be imaged was successively changed. A pipet tip (ZAP premier 200 µL pipet tip, VWR) was filled with radiopaque dye and placed behind the tissue container and imaged with the skin block. A schematic of experimental set up is shown in Fig. 3-8.

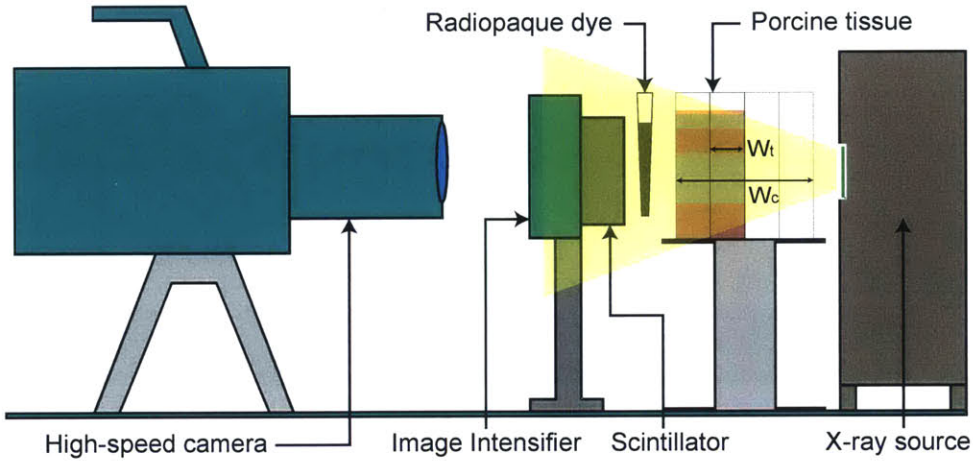

Figure 3-8: A schematic of high-speed X-ray imaging experimental set up for imaging a tissue with different widths and a radiopaque dye.

High-speed X-ray videos were taken with a source current of 500 mA, source voltages of 40 kVp, 50 kVp, 60 kVp and 70 kVp at different exposure times of 1000 fps (frame/s), 1500 fps and 2000 fps. MATLAB (MATLAB 2014B, The MathWorks,

Inc.) [42] was used for post-image processing of the X-ray images. Each image file was converted into a grey scale image with 8-bit resolution. A local contrast between the radiopaque dye and tissue, a background noise as the noise of tissue area in an x-ray image and SNR, described in section 2.5.2, were calculated based on the image values of each pixel to evaluate the image quality.

3.3.2 Effect of Source Voltage and Tissue Width on Image Quality

X-ray images of different source voltage and tissue widths are shown in Fig. 3-9. Increasing the source voltage made the images brighter, which indicated that more X-ray beams penetrated the tissue and arrived at the scintillator plate.

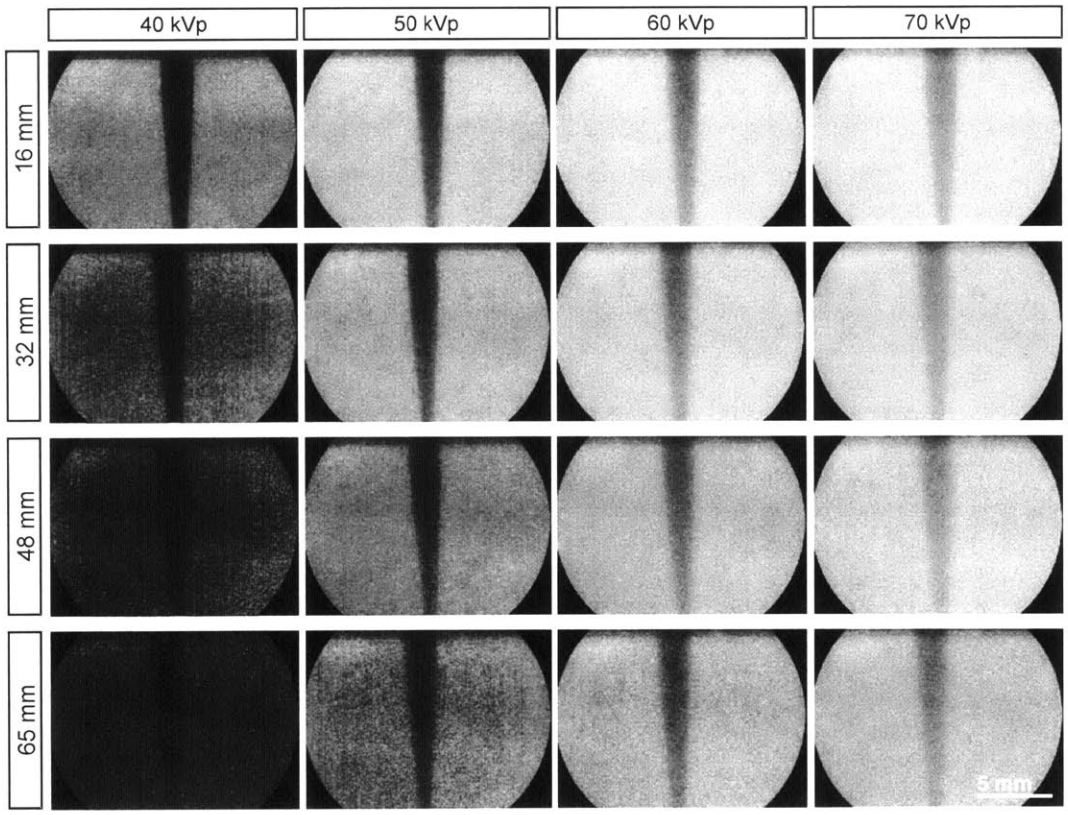

Figure 3-9: X-ray images of different source voltage and tissue widths.

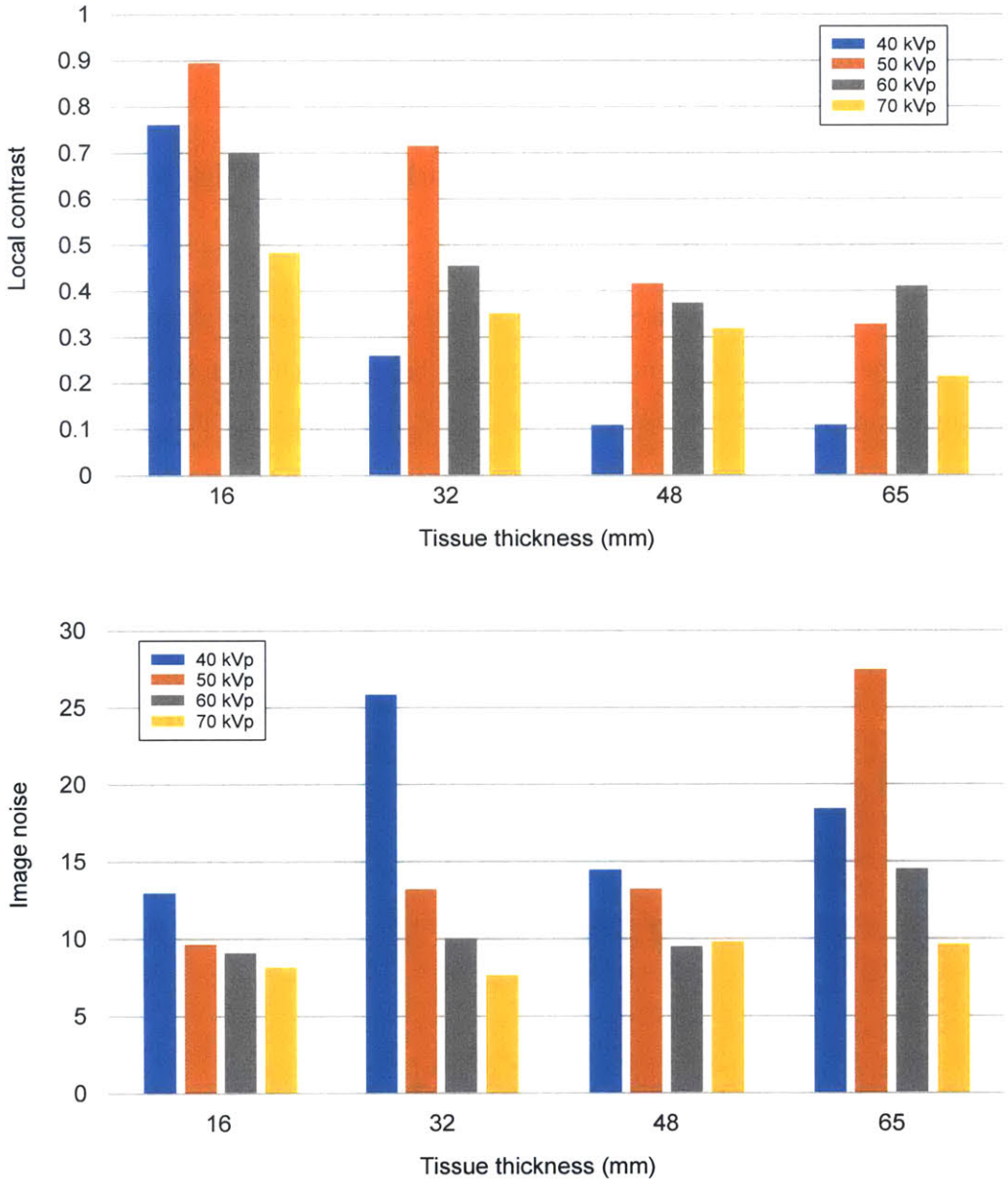

Figure 3-10: Effect of source voltage on the local contrast (top) and the image noise (bottom) of the X-ray image for different tissue widths.

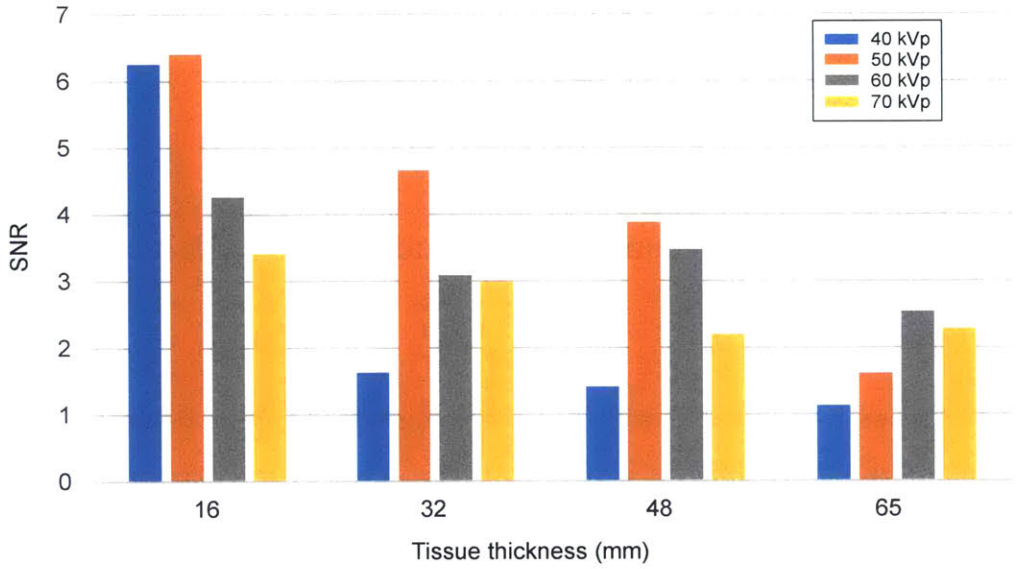

Figure 3-11: Effect of source voltage on SNR (signal to noise ratio) of the X-ray image for different tissue widths.

Fig. 3-10 shows the effect of the source voltage on the local contrast and image noise with tissues of different widths. As is shown, the peak of the local contrast differs with tissue width. For a tissue width of 16 mm, 32 mm and 48 mm the contrast peaked at 50 kVp whereas the contrast peaked at 60 kVp for a 65 mm tissue width. The image noise decreased in all tissue widths except for 65 mm, as the source voltage increased. This decrease can be explained using the same argument that was used to explain the increase in brightness of images. The fact that the effect of the source voltage on the local contrast and the noise for each tissue width varies means the value should be optimized for each tissue width. For example, for tissue with a width of 65 mm, approximately 50 kVp is the range where the contrast, C, is relatively high but the image noise is in the background is high (see Fig 3-10).

To find the optimal source voltage, SNRs of different tissue widths were calculated, as shown in Fig. 3-11. As can be seen the SNR is generally high with narrower tissue blocks as X-ray beams that passed through narrower block of tissue were higher in intensity. In addition, an optimal source voltage exists for each tissue width. The SNR peaked at 50 kVp for tissues having width of 16 mm, 32 mm and 48 mm, while

it peaked at 60 kVp for tissue that was 65 mm wide. The peak SNR tends to move towards the higher source voltage as the tissue block gets wider.

3.3.3 Effect of Exposure Time and tissue width on Image Quality

Fig. 3-12 shows X-ray image,s with a source voltage of 50 kVp, of tissue blocks with different widths using different exposure times. As is shown, the image becomes darker as the exposure time increases since less light is collected by the camera for each frame.

Fig. 3-13 shows the effect of exposure time on the local contrast and image noise. The relationship between exposure time and local contrast is not clear. For tissue blocks with a width of 16 mm, the contrast increases as the exposure time decreases, but an opposite trend is observed in tissues with widths of 48 mm and 65 mm, and still a different trend in the tissue of a 32 mm width. The relationship between the exposure time and local contrast is not clear and may reflect the fact that the local contrast is mainly determined by the energy of the beam and not by the number of X-ray photons, as discussed in Section 3.2. However, the effect of the exposure time on the image noise is clearly shown. As the exposure time decreases, the noise increases since there is less light collected by the camera.For images of tissues with width of 16 mm, the noise in each exposure time is comparable, which suggests that a source voltage of 50 kVp and source current of 500 mA is high enough intensity that it is not affected by the exposure times used in the experiment.

The calculated SNR in Fig. 3-14 shows that a higher exposure time will give a better image quality in general. In addition, the effect of exposure time on SNR becomes more noticeable in a wider tissue block, suggesting that exposure time has more effect on the image quality when the tissue block is wider, as it is expected from the Equation 3.3.

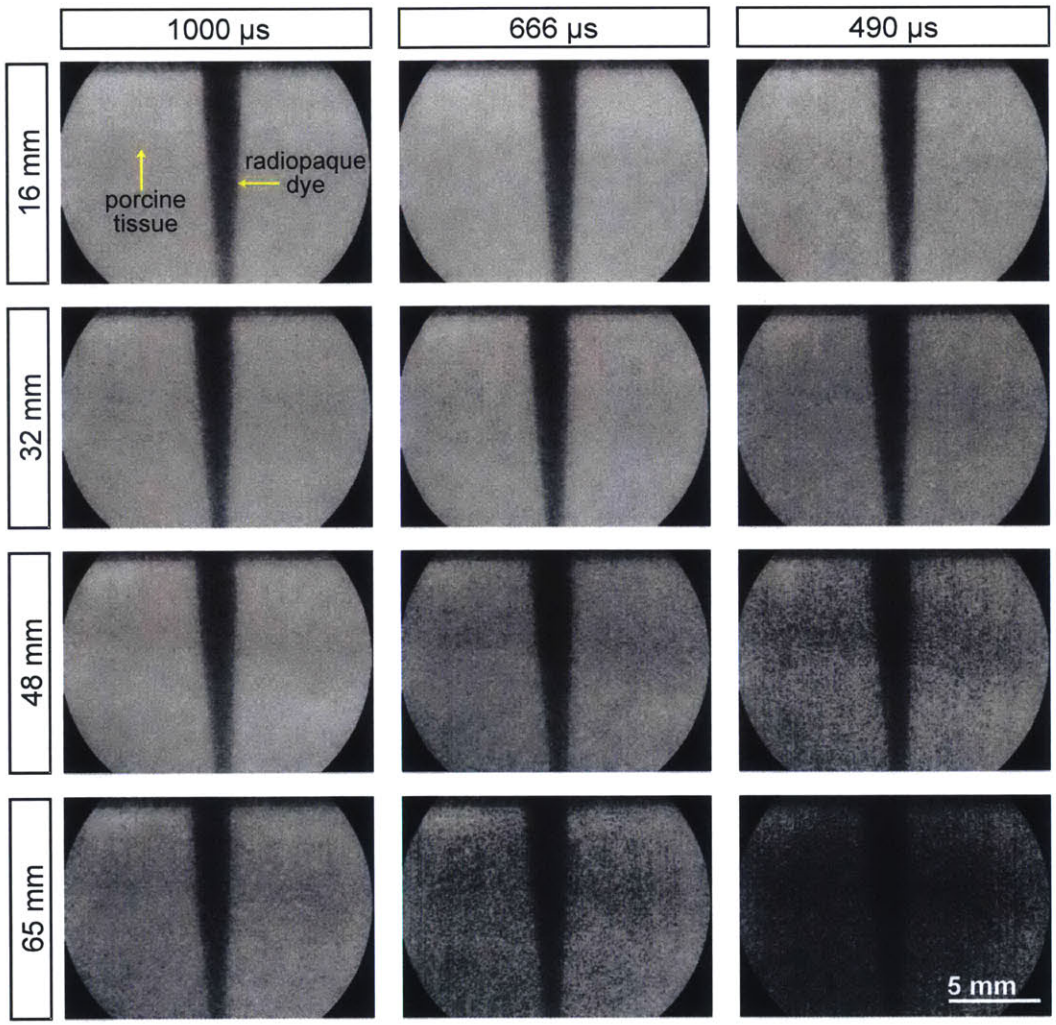

Figure 3-12: X-ray images of different exposure time and different tissue widths.

3.3.4 High-Speed X-ray Imaging of Large Tissue Block

To verify the effect of the exposure time and the source voltage on the image quality of a jet injection of large tissue blocks, a tissue block of 65 mm width was injected with 100 µL of contrast agent and the injection was imaged in real time using the high-speed X-ray system. A source voltage of 60 kVp was chosen give the optimal SNR. Although 1000 fps gives the best SNR, 1500 fps was chosen as permitted collection of more information about the dynamics of jet dispersion in real time, as discussed in Section 3.2.

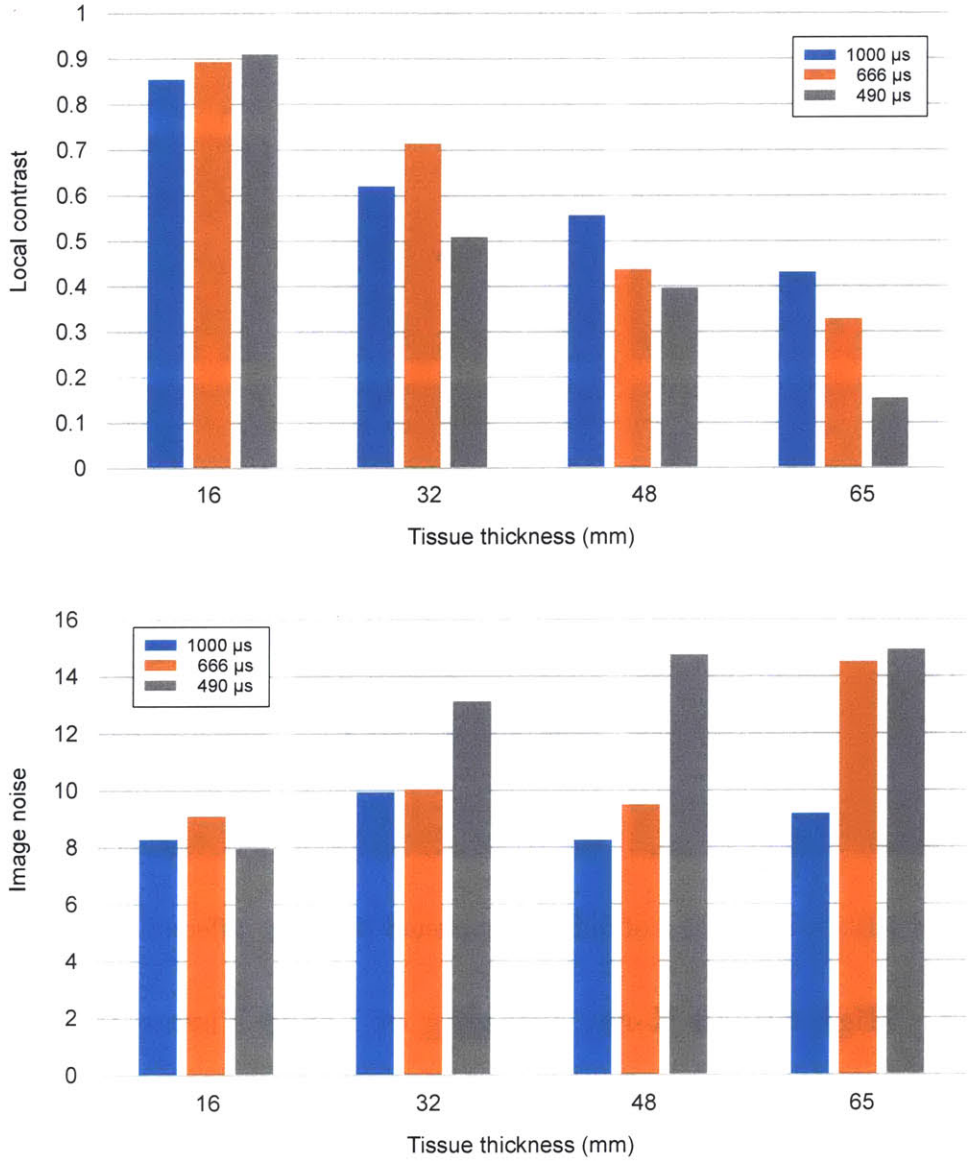

Figure 3-13: Effect of exposure time on the local contrast (top) and the image noise (bottom) of the X-ray image for different tissue widths.

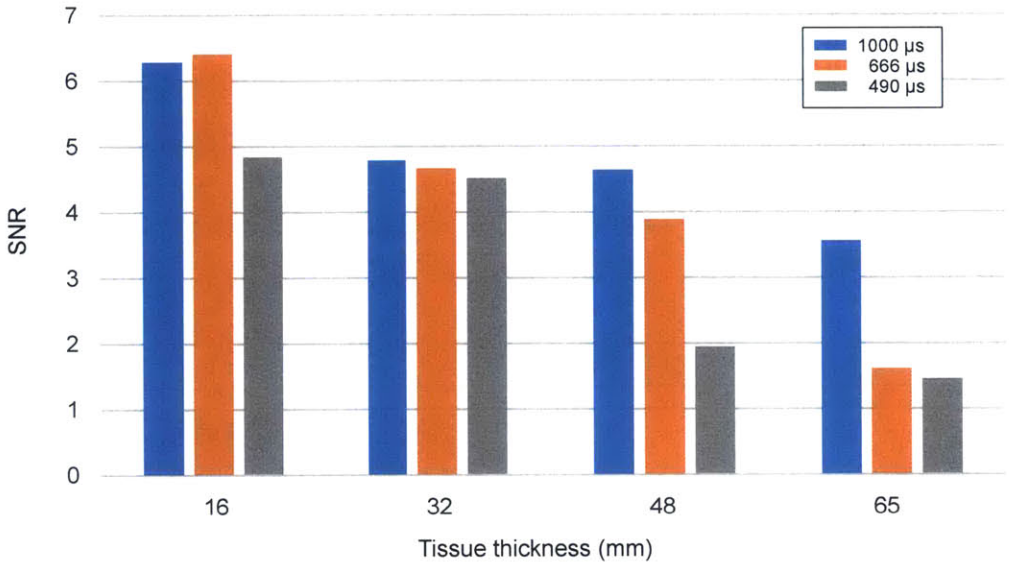

Figure 3-14: Effect of source voltage on the SNR of the X-ray image for different tissue widths.

Fig. 3-15 shows the X-ray and post injection images of a jet injection into a tissue block 65 mm wide and as compared to injection into a tissue block 22 mm wide. As can be seen, the X-ray images of 65 mm width tissue block have more noise than those of a smaller block. The calculated image noises, a standard deviation of image values of tissue area, for each injection were 16.7 for 65 mm width tissue block and 9.4 for 22 mm width tissue block. Although the jets in both injection reached to the muscle layer the contrast agent inside the 65 mm width tissue block is hard to recognize, while that of a smaller block shows several small streams of a fluid branching out of the initial bolus. A previous study on the X-ray imaging of the jet injection indicated that streams of the injectate were founded in the dispersion pattern of the jet as it preferentially flow throught the weak cells [28]. Hower, compared with the post injection image, X-ray images of 65 mm width tissue cannot provide the information about jet injection dispersion pattern that can be correlated to with the post injection images.

Furthermore, each layer of the skin in the 65 mm width sample is less distinguish-

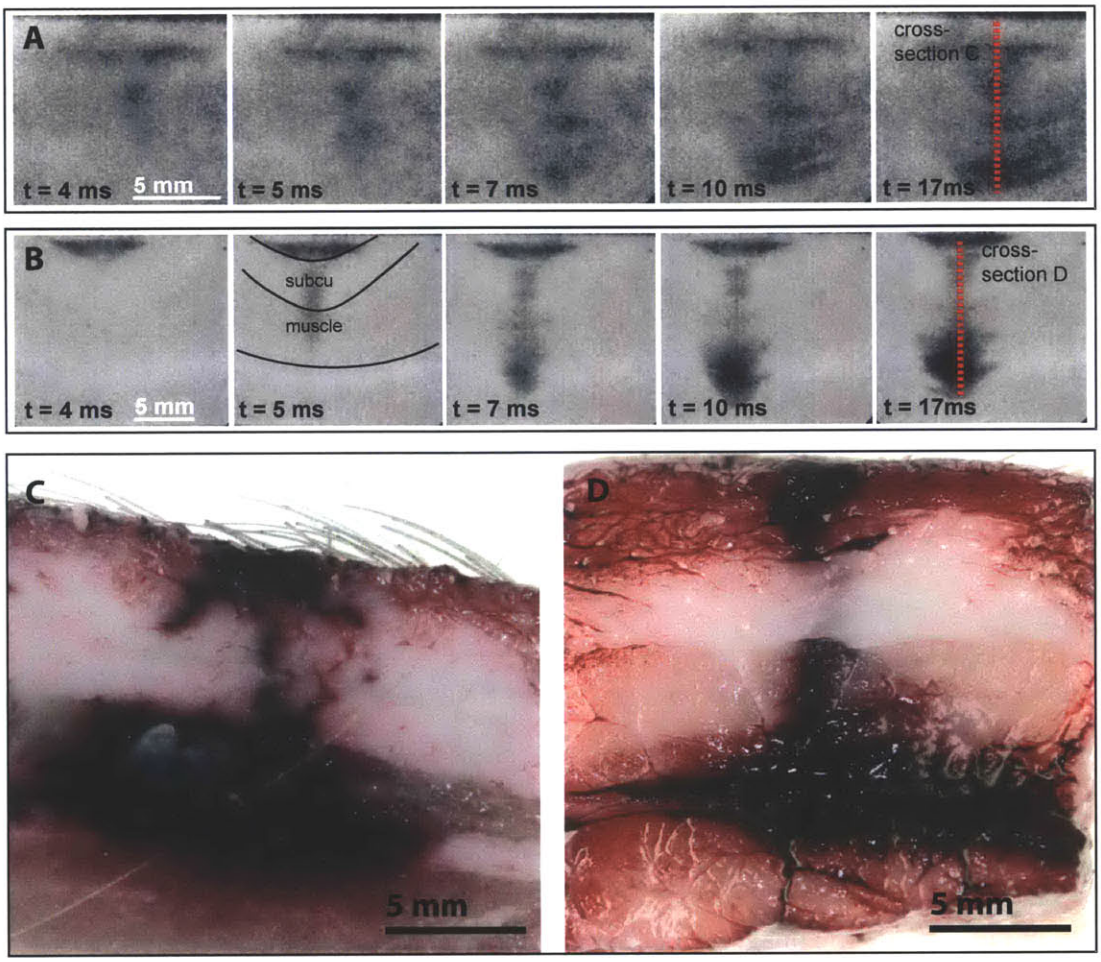

Figure 3-15: Frames from X-ray videos of jet injections into tissue with different dimensions, 80 mm × 65 mm (L×W) × 30 mm (H) (A) and 22 mm × 22 mm (L×W) × 18 mm (H) (B). Images of tissue samples medially sectioned along the red dashed line for the large block (C) and the small block (D). "Subcu" indicates the subcutaneous adipose layer.

able compared to that in smaller imaging width. This result suggests that images of 65 mm width lack local contrast between each layer and have high noise, resulting in SNR too low to give sufficient information about the tissue structure. Therefore, it is concluded that increasing the exposure time and source voltage cannot completely solve the problem of imaging a wider tissue in the previous high-speed X-ray imaging system.

Figure 3-16: Images showing the tissue deformations of 80 mm × 30 mm (L×W) × 30 mm (H) size tissue block, when the ampoule applied pre-load.

3.3.5 Asymmetric Tissue Block

Another solution left to the problem is to upgrade the source to a higher source current, which will allow the X-ray source to increase the number of X-ray photons without sacrificing the exposure time. However, an X-ray source that has a higher source current with the same focal spot size will cost well over $150,000, as it requires an additional mechanism to deal with the heat generated from the anode, as discussed in Section 2.5.2.

Therefore, an alternative approach which involved using an asymmetric dimension for the tissue block was taken to avoid the problem. By using asymmetric dimensions, the tissue block can have a thin enough depth in one dimension to get high image quality and a wide enough length in the other dimension to obtain reasonable stress distribution and deformation of tissue. However, one drawback of using asymmetric dimensions is that it might generate an asymmetric dispersion pattern because of the asymmetric boundary condition in two different dimensions.

To investigate the effect of using an asymmetric dimension, four jet injections were made into a tissue block of 80 mm × 30 mm (L×W) × 30 mm (H) with the system parameters optimized in Section 3.3.2 and 3.3.3. A length of 80 mm was chosen based on the observation of the tissue deformation when the contact force was applied (Fig. 3-1).

In addition, it was assumed that the advantage of having a short time resolution

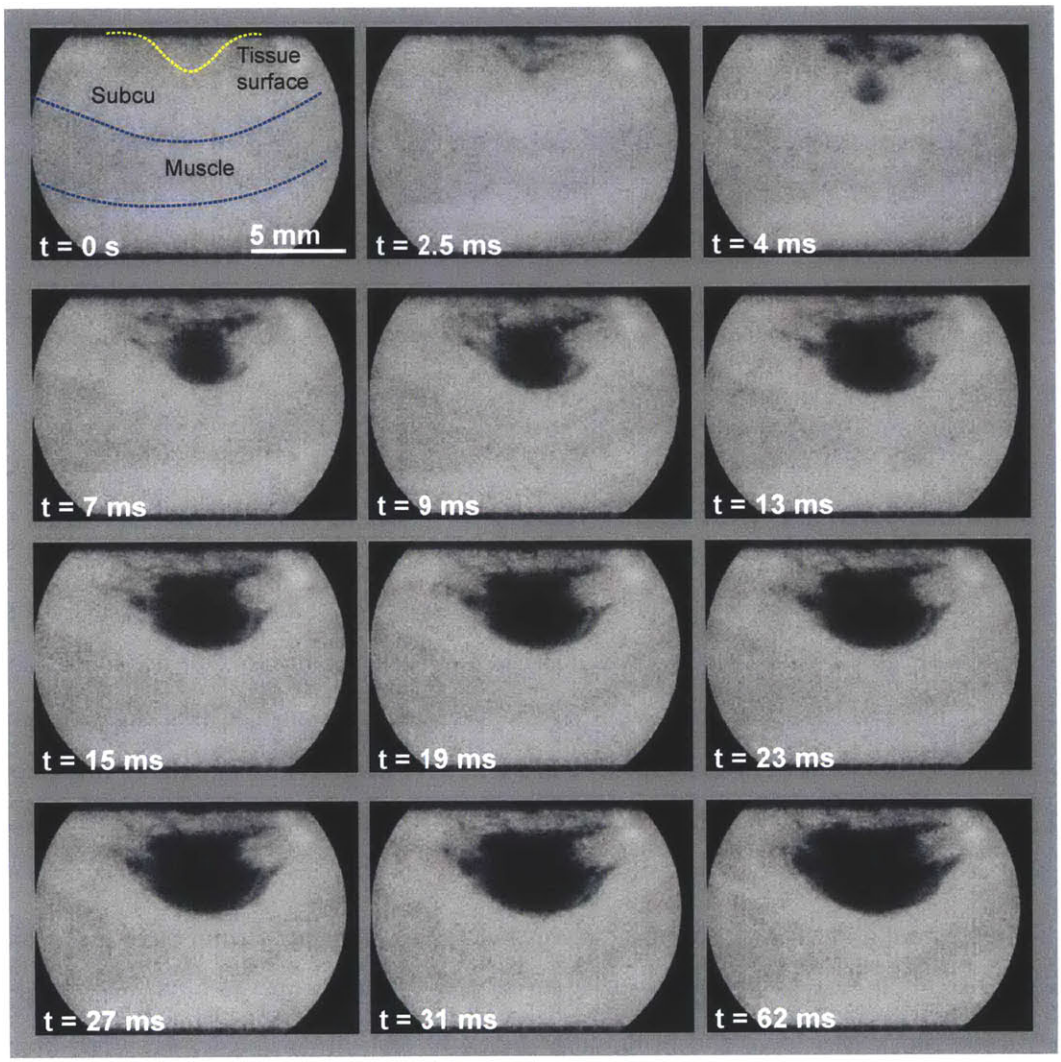

Figure 3-17: Frames from X-ray videos of the jet injection into 80 mm × 30 mm (L×W) × 40 mm (H) size tissue. Set parameters: v_{jet} = 200 m/s, v_{ft} = 50 m/s.

with high enough quality was greater than the advantage of having a wider tissue. As can be seen in Fig. 3-14, having a shorter exposure time in the 48 mm width tissue block would decrease SNR more significantly than in the 32 mm width tissue block. Therefore, a width of 30 mm was chosen, as representative of the 32 mm width block discussed in the previous section, rather than the length around 48 mm. Parameters for the jet injections were kept constant between injections with a v_{jet} of 200 m/s, t_{jet} of 10 ms, v_{fol} of 50 m/s and contact force of 1 N.

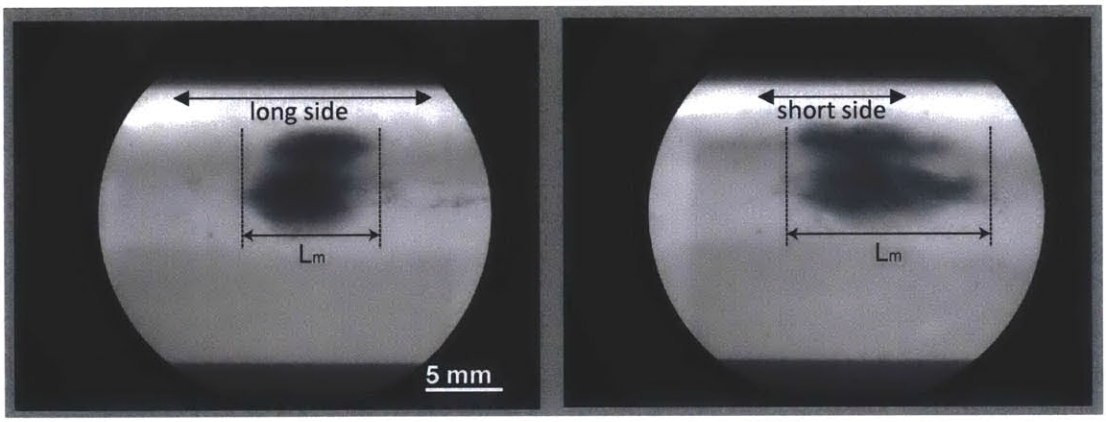

Figure 3-18: X-ray images of the jet injection into 80 mm × 30 mm (L×W) × 30 mm (H) size tissue block. A left image shows the jet dispersion in the direction of long side of the tissue and a right images shows that in the direction of short side of the tissue. X-ray images were taken with a source current of 500 mA, a source voltage of 40 kVp, at a frame rate of 10 fps with an exposure time of 9 ms.

Fig. 3-16 shows the deformation of the asymmetric tissue when the surface of tissue was pressed by the same amount of displacement as the setup shown in Fig. 3-1. When compared to the surface deformation observed using other dimensions, tissue block of 80 mm × 30 mm (L×W) × 30 mm (H) displayed more similarity of deformation patterns to those observed for the larger block in Fig. 3-1A than that of the smaller block did in Fig. 3-1B. This suggested that the boundary conditions experienced in the asymmetric block were more comparable to those in the larger block than those in the smaller block was.

In addition three jet injections of raidopaque dye into an asymmetric tissue block were made and imaged using the high-speed X-ray imaging system. Fig. 3-17 shows X-ray images of one jet injection. High-speed X-ray imaging of jet dispersion suggests that the image quality was comparable to that shown in Fig. 3-15B. The fluid paths inside the subcutaneous fat layer, including the streams, had high enough local contrasts with low enough noise to make it distinguishable from the tissue. In addition, each layer of the tissue was visible in the images.

However, jet dispersions of injections showed evidence of asymmetric dispersion pattern. After injection, the width of the maximum dispersion was measured by the

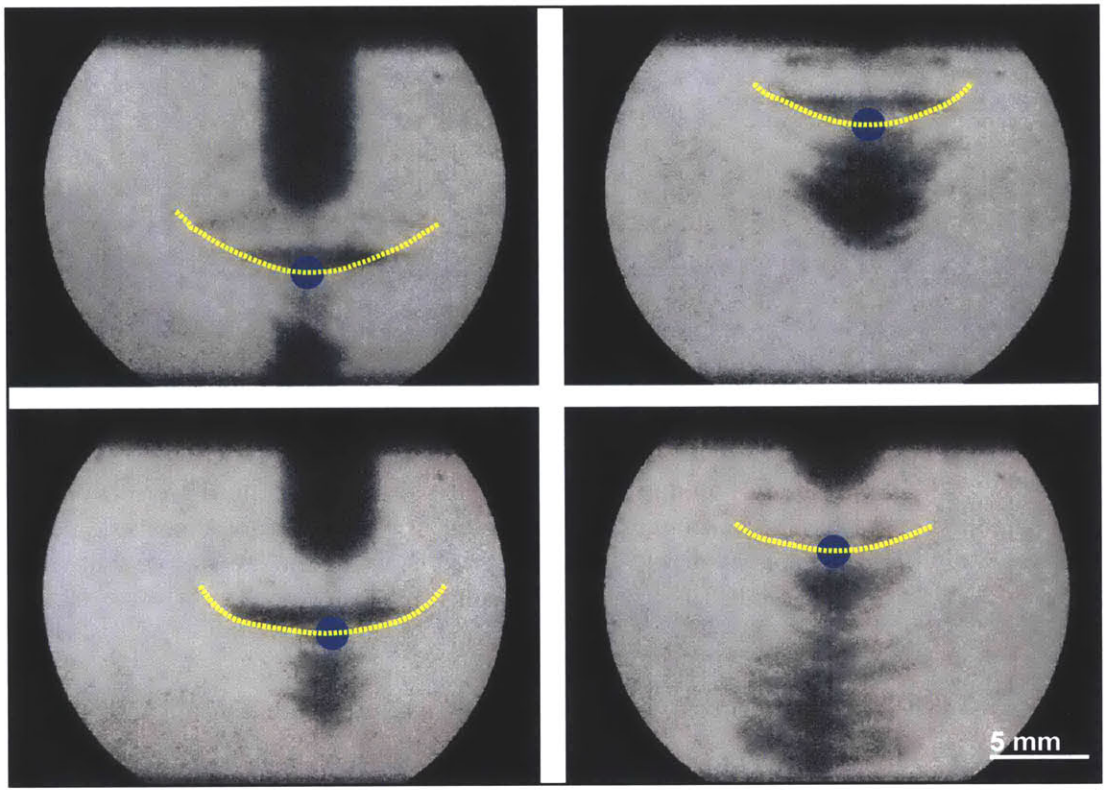

Figure 3-19: X-ray images of different jet injections showing the different positions of the ampoule. Yellow dashed lines indicate the tissue surface and blue dots indicate the position of the nozzle.

X-ray imaging system with a long exposure time as shown in Fig. 3-18. The average maximum width in the direction of the long side was measured as 5.02 mm $\pm$ 0.75 mm and the average width in the direction of the short side was 6.34 mm $\pm$ 0.89 mm, possibly indicating that the jet dispersion tended to favor the direction of the short side. However, this unnatural bias was considered to be acceptable, given the fact that the dispersion width with symmetric tissue block shows similar range of variance.

From these results, it is concluded that using an asymmetric dimension for tissue block will help improve the stress distribution and deformation of the tissue in jet injection experiment into the porcine tissue while maintaining the image quality, with a possible defect of asymmetric dispersion pattern.

3.4 Hardware Modifications to the Previous High-Speed X-ray Imaging System

The experimental hardware setup for the high-speed X-ray imaging system was modified to accommodate tissue blocks with dimensions considered to be optimal based on the results presented in Section 3.3. This involved modifications of the jet injector mount and tissue mount.

Injector Mount

One difficulty in using the previous high-speed X-ray imaging system was that the tip of the jet injector, a main object in the image, moved relative to the fixed high-speed camera. This occurred because the injector was mounted on a vertical linear stage so that the tip of the ampoule could apply the required contact force by sitting on the surface of tissue placed on a stationary mount. Depending on the

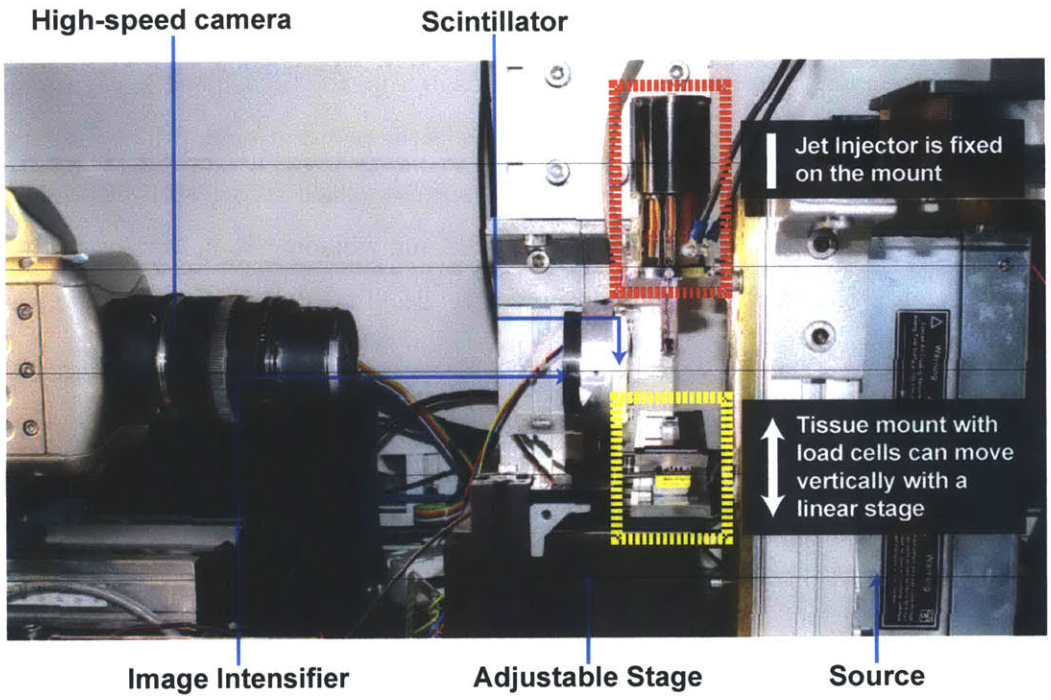

Figure 3-20: The high-speed imaging system fro needle free jet injector. The sample to be injected is placed on the force sensor. By raising the adjustable linear stage under the force sensor, pre-load is applied to the tissue surface from ampoule tip.

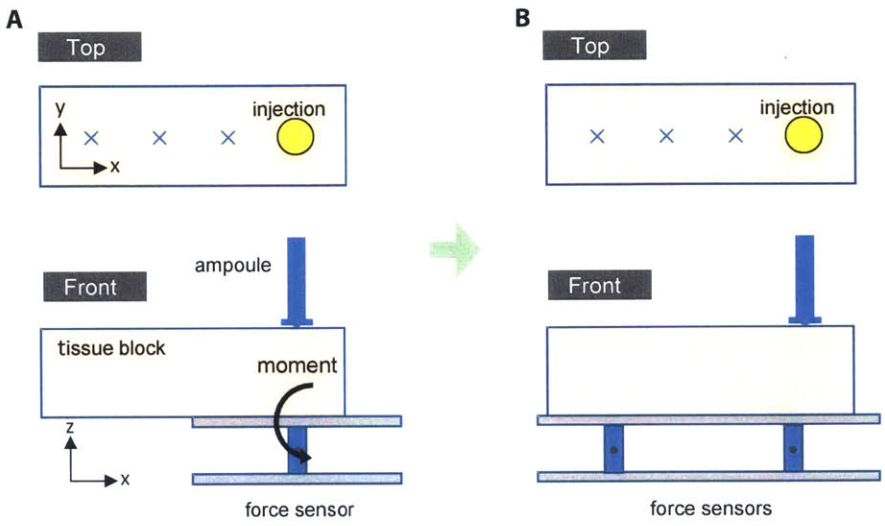

Figure 3-21: (A) Diagram showing the moment is being applied by the larger block to the previous tissue mount. (B) Modified tissue mount using two load cells.

height of tissue block and the applied contact force, the position of the ampoule varied significantly in the image as shown in Fig. 3-19.

Considering that the window size of the image from the high-speed X-ray imaging system is only 30 mm (H) by 40 mm (W), whereas the penetrating depth of the typical intra-muscular jet injection reaches up to 40 mm, position changes in ampoule can make the imaging subject deviate from the imaging window. To solve this problem, the jet injector was fixed on the mount and a vertical linear stage was installed under the tissue mount stage as shown in Fig. 3-20.

Tissue mount and Force sensor

Another issue with the previous set up was the tissue mount stage that contained a load cell. The stage was designed for jet injection using small tissue blocks, where only a single injection was made into each block. However, since several injections are made into the larger tissue block, the previous tissue mount could generate a moment on the plate on which the tissue sat as described in Fig. 3-21. Thus, the contact force applied from the tip of an ampoule could not be measured accurately using the previous hardware experimental set up. Instead of using a single load cell, two load cells (LSB 200, Futek) [43] were installed between the two plates to avoid generating

a moment on the plate.

THIS PAGE INTENTIONALLY LEFT BLANK

Chapter 4

Effect of Contact Force on Critical Stress

Jet injection using commercial jet injection devices is conducted by making contact between the nozzle of the ampoule and the injection site, which suggests that jet injections into a human body are always performed with a non-zero contact force from the device. However, not many studies have been done tha evaluate the effect on jet injection by contact force. One study showed that applying a higher contact force might result in deeper penetration of the jet [28]. This previous work conjectures that the reason for deeper penetration with the presence of a contact force is pre-stretching of the skin. There are several studies suggesting that pre-stretching might have an influence on the needle injections and knife insertions into skin, but the results are not consistent [28].

Since pre-tensioning the skin changes the stress distribution on the skin surface, it is natural to assume that pre-tensioning will change the critical stress of the skin and therefore have an influence on the dispersion pattern. The critical stress for failure under uniaxial tension of procine skin was determined to be about 15 MPa [44]. Since the failure of the skin in this study was a result of tearing of a surface, rather than penetration by a jet, it is difficult to interpret it as the critical stress of skin by the jet. Baxter and Mitragotri showed that the critical stress of jet injection into the porcine tissue (derived from the model) ranged between 0.46 to 5.8 MPa, depending

on the Young's modulus of the skin [22]; admittedly these values were less than those reported in the literature. However, the critical stress was measured from the jet velocity using Bernoulli's steady equation under the assumption of no energy loss, and the measurement of the breaching time was limited by their imaging system.

Given the range of critical stress values in the literature, additional studies are required to determine the effect of contact force on jet injection. This chapter uses a high-speed X-ray imaging system to investigate the effect of contact force on the critical stress of porcine skin using a high-speed X-ray imaging system.

4.1 Experimental Method

One advantage of using a high-speed X-ray imaging system to investigate the mechanism of jet injection is that the breaching time of tissue can be visualized in the X-ray image. Both the deformation of the tissue surface and the fluid flow of radiopaque dye can be observed. These observations together with knowledge of the jet force and the geometry of the nozzle permit an estimation of the critical stress for failure.

The relationship between the contact force and the critical stress of porcine skin by the jet was investigated by comparing two experiments: jet injections into porcine tissue with and without the contact force. High-speed videos of the injections were taken, and the jet force of the ampoule used in the experiments was measured. By relating the profile of jet force with the X-ray video which captured breaching moments of jet injection, the critical stress of the skin was estimated for each injection.

4.1.1 Jet Injection Preparation

*Ex vivo*porcine abdominal tissue was prepared as described in Section 3.3.1, and all injections were performed using Injex 30 ampoules (INJEX Pharma) [5]. The Lorentz force needle free jet injector was used to inject a fluid volume of 100 μl with injection parameters of v_{jet} = 200 m/s and v_{fol} = 50 m/s. For injections with contact force, the jet injector applied a contact force of 1.0 N onto the skin surface.

To obtain sufficient knowledge about the breaching moment of the jet, it is important to identify the skin surface, ampoule and injectate in the X-ray image. However, X-rays can easily penetrate the skin surface and the ampoule with the optimized X-ray source parameters for the imaging set up, it is difficult to distinguish the tissue surface and the ampoule tip in the X-ray image. As a solution to the problem, a silver paint (, Structure Probe Inc., Flash Dry Silver Paint) [?] was used to increase the visibility of the skin surface and the ampoule in X-ray image. An ampoule was coated with the paint and a line with 2 mm width and 65 mm length was drawn on the skin surface using the same paint, as shown in Fig. 4-1. In addition, the radiopaque dye (AuroVist-15 nm, Nanoprobes) [45] was diluted to 10% to reduce the visibility and thereby, differentiate the skin surface from the injectate pooled on the surface. High-speed X-ray videos were taken with a source voltage of 40 kVp, tube current of 500 mA, at 2000 fps with an exposure time of 500 μs.

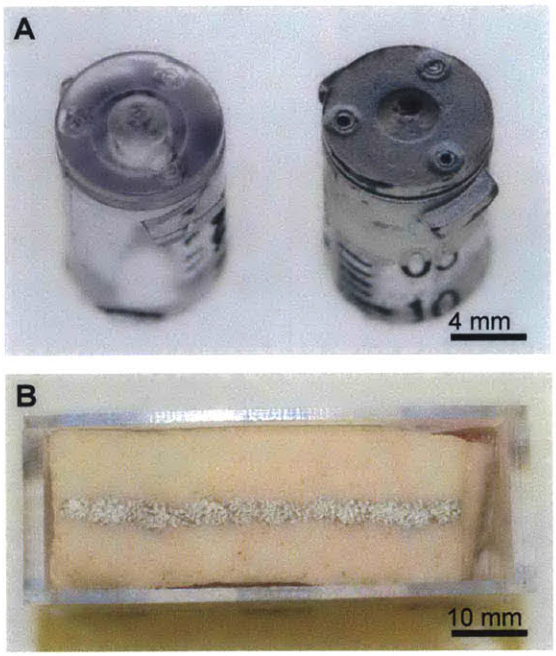

Figure 4-1: (A)Tip of a normal ampoule (left) and silver-coated ampoule (right). (B) A line was drawn with the silver paint on the surface of tissue.

4.1.2 Jet Force Measurement

Jet force was measured in an experiment setup shown in Fig. 4-2. The injector with an ampoule was placed above a load cell (LSB 200, Futek) with a stand-off distance of 1 mm, 5 mm and 10 mm from the top plate of the load cell. The injector ejected water onto the load cell with jet parameters of v_{jet} = 200 m/s, t_{jet} = 10 ms and v_{ft} = 50 m/s, and data were recorded using the National Instruments Compact RIO system described in Section 2.2. The jet pressure was calculated by dividing the nozzle area of the ampoule assuming the jet had a collimated stream. To verify that the jet stream is collimated, high-speed video of a water ejection was taken at frame rate of 6400 fps with and exposure time of 156 μs.

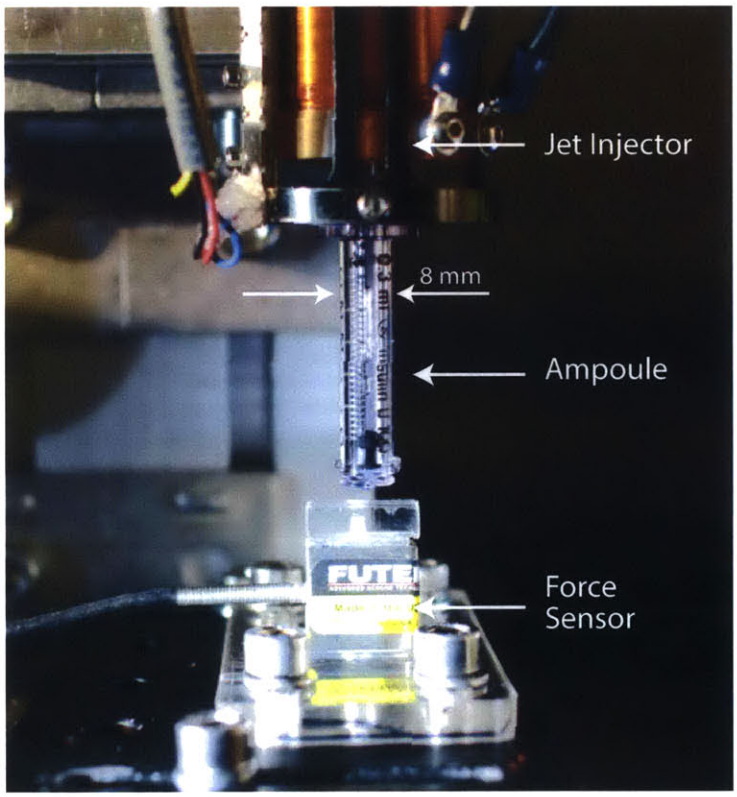

Figure 4-2: Experiment setup for the jet force measurement.

4.2 Experimental Result

4.2.1 Jet Force

Fig. 4-3A shows jet pressures, calculated from measured jet force, with different stand-off distances from the top plate of the load cell. Intuition suggests that a jet force at a long stand-off distance will show a time delay compared with that of a short stand-off distance because of traveling time. However, since the jet has a high acceleration and speed, the jet pressure profiles at different stand-off distances shows delays of 0.5 ms and 0.7 ms only at the beginning (see Fig. 4-3B). Thus, jet pressures at a stand-off distance within 10 mm can be assumed to have comparable profiles.

Fig. 4-4 shows calculated jet pressure with corresponding calculated coil velocity of a water ejection with 1 mm stand-off distance. The first peak of the jet pressure reached approximately 20 MPa at t = 4.6 ms and oscillated with approximately 5 MPa peak to peak amplitude at about 277 Hz frequency during the time at v_{jet}. During the v_{fol} period, the jet pressure decreased to 1.5 MPa and oscillated at about 1.11 kHz frequency with less than 0.6 MPa peak to peak amplitude. The velocity curves in Fig. 4-4 show that peak velocity was reached at t =3.3 ms, 1.3 ms before peak pressure. In addition, the magnitude of the peak decreased by 52.1 % at the second peak in coil velocity, while the jet pressure only decreased by 6.2 %. This suggests that even though the coil drives the jet, the coil dynamics does not fully reflect the jet dynamics, in part because of the compliance associated with the rubber piston tipis mainly because of the rubber tip of the piston in contact with the fluid [46]. Therefore, the jet pressure profile, rather than coil velocity profile, needs to be used to analyze the jet dispersion in real time.

4.2.2 Without Contact Force

The X-ray images for jet injection without contact force are shown in Fig. 4-5. In the X-ray image at time t = 0 sec, the ampoule was seated up on the top of the skin surface with no application of force. As the injection began, the jet stream exiting

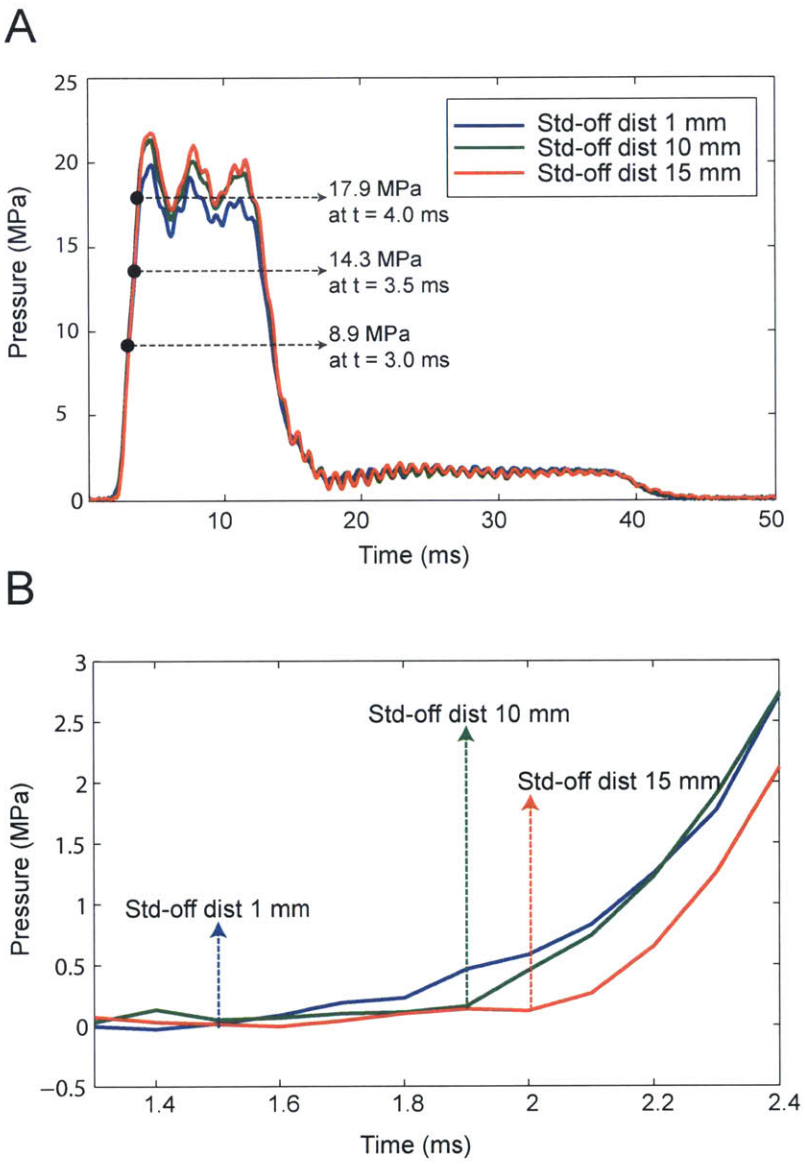

Figure 4-3: (A) Measured jet pressures with different stand-off distances. (B) Stand-off distance 10 mm and 15 mm showed delays of 0.5 ms and 0.7 ms, respectively.

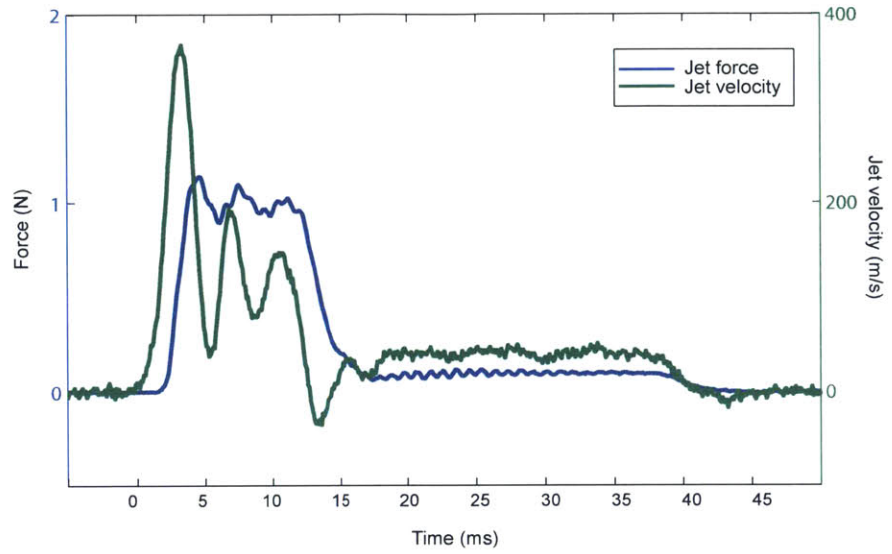

Figure 4-4: Measured jet pressure and calculated jet velocity at a stand-off distance of 1 mm.

the nozzle of the ampoule deformed the tissue surface until it breached the surface, and fluid was injected into the skin at t = 4.0 ms.

As is shown in Fig. 4-3, the jet pressure at the breaching time, t=4.0 ms, was 17.9 MPa. However, considering that the imaging time resolution was 0.5 ms, the jet pressure at the breaching time can range from 14.3 MPa to 17.9 MPa. The critical stress of the jet injection without the contact force, which can be approximated as calculated jet pressure, is comparable to 15 MPa, the critical stress of the porcine skin reported in previous study [44].

The injectate appeared in the images as a dark bolus under the tissue surface. As the bolus expanded, the surface around the injection hole swelled to form a welt indicating that fluid had infiltrated the dermal layer. The skin surface moved toward ampoule as the coil velocity reached v_{fol} and finally retracted back to its original position when the injection ended at t = 65 ms.

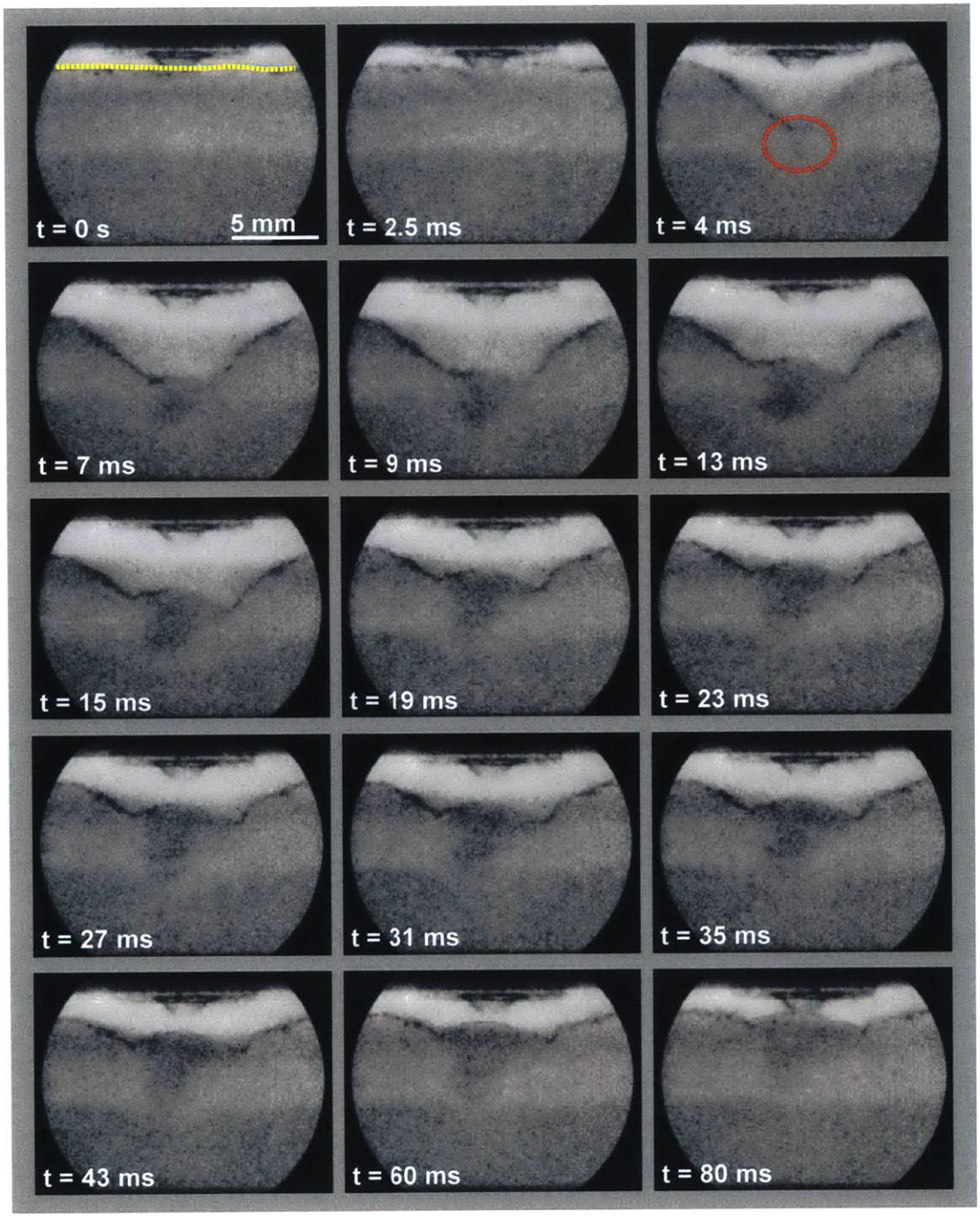

Figure 4-5: Frames from X-ray videos of the jet injection without a contact force. A yellow dashed line indicates the surface of the tissue and a red dashed line indicates the first entry of injectate into the tissue.

4.2.3 With Contact Force

Fig. 4-6 shows the X-ray images of a jet injection where a contact force of 1 N was applied to the tissue. Unlike the injection without contact force, the tissue surface showed no significant deformation during the injection. The breaching of the surface occurred at t = 3.5 ms, 0.5 ms earlier than without the contact force. The calculated jet pressure at the breaching time was 14.3 MPa, which again can range from 9.9 MPa to 14.3 MPa. The critical stress of the jet injection with the contact force was at most 3.6 MPa less than that without a contact force. This means that contact force of 1 N provided the pre-stretching of at most 8 MPa to the tissue surface, which helped the jet breach the surface of the skin at a lower jet pressure than without the contact force.

The jet dispersion patterns for injections done in the absence or presence of a contact force are shown in Fig. 4-7. After jet injections, the tissue block was frozen at -20 °C, medially sectioned, and photographed. In the jet injection with contact force, the jet reached up to the boundary between subcutaneous fat and muscle layer, whereas the jet only reached the subcutaneous fat layer in the jet injection without contact force. The variation in the dispersion depth could be because the jet in the absence of a contact force had to spend extra energy to deform the tissue surface before it breached it, while in the presence of a contact force such energy was provided by the contact force.

Furthermore, the jet dispersion pattern in the presence of a contact force had a bolus shape, the center of which was located in the subcutaneous layer. The dispersion pattern in the absence of a contact force was cone-shaped. The variation in the dispersion pattern may be due to the stand-off created by the deformation of the tissue in the absence of a contact force. Given that the jet stream is not a perfect cylindrical shape with constant diameter, a stand-off between the ampoule tip and tissue surface could cause the jet to deviate from the breached hole, which resulted in the loss of injected volume and corresponding momentum.

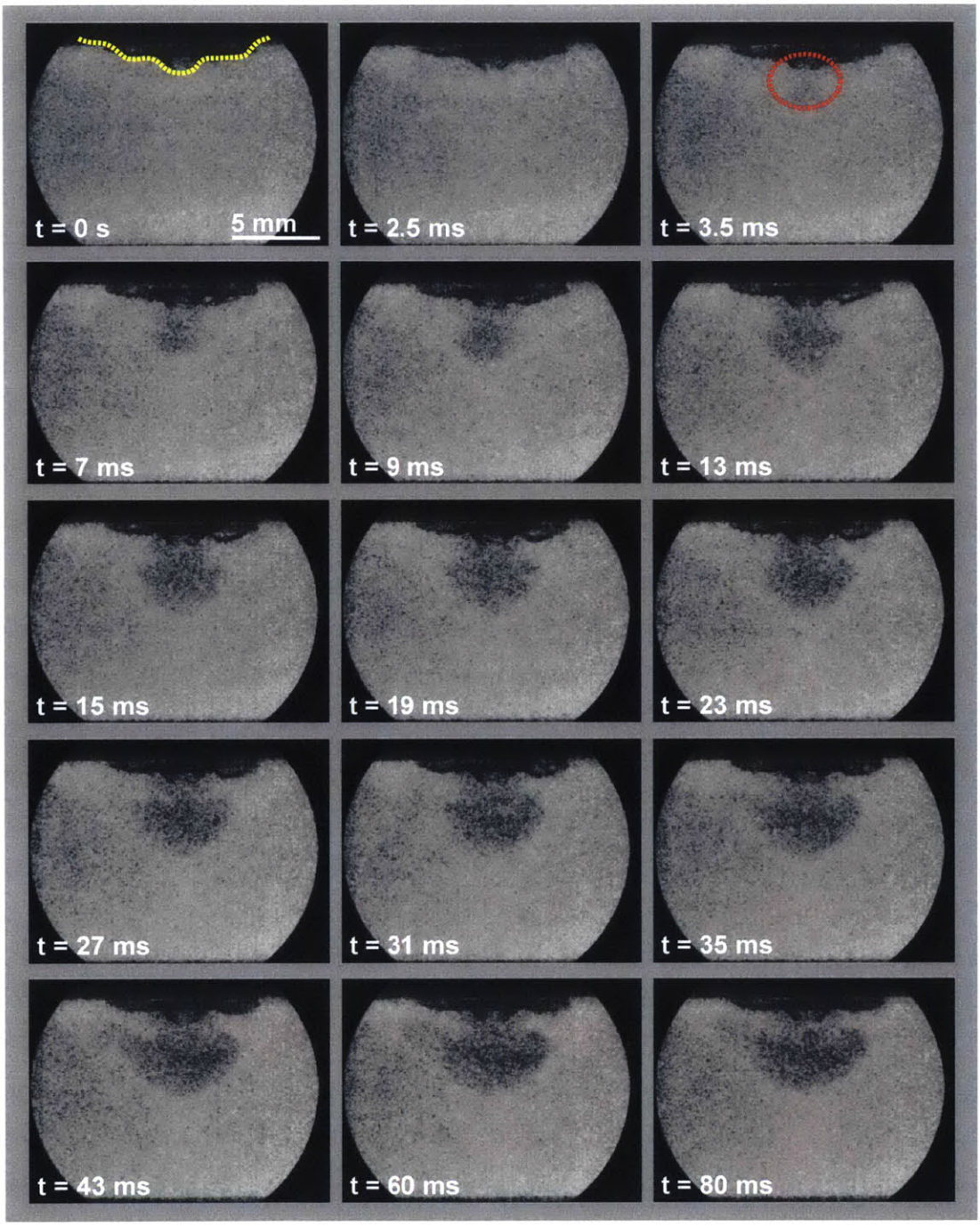

Figure 4-6: Frames from X-ray videos of the jet injection with a contact force. A yellow dashed line indicates the surface of the tissue and a red dashed line indicates the first entry of injectate into the tissue.

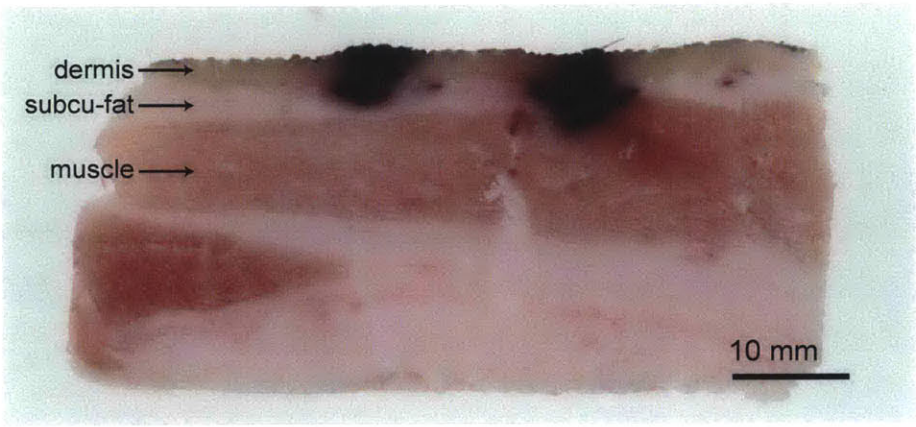

Figure 4-7: Image showing the dispersion pattern of the jet injections without (left) and with (right) a contact force.

4.3 Conclusion

High-speed X-ray videos of the jet injections were taken to investigate the effect of contact force on the critical stress of porcine tissue by a pressure fluid jet. Real-time images of injections were compared with the jet pressure profile measured in a separate experiment. The presence of a contact force reduced the jet pressure required to breach the skin surface and resulted in deeper penetration of the jet into the tissue. It is hypothesized that skin pre-tensioning generated by the contact force and preservation of the contact between the ampoule tip and tissue surface can improve delivery of the injectate into the tissue.

THIS PAGE INTENTIONALLY LEFT BLANK

Chapter 5

Effect of Jet Shape on Jet Dispersion

Previous studies on the mechanism of jet injection are all based on a jet stream model with collimated shape, with the assumption that the jet shape does not change. However, given the fact that the shape of the jet stream represents the direction of the fluid coming out of the nozzle, jets with equivalent jet power, but with different jet shapes, can lead to different jet dispersion mechanisms. Therefore, the effect of the jet shape must be taken into account as another important parameter determining the jet dispersion mechanisms of jet injection. In this chapter, the effect of jet shape is evaluated by comparing dispersion and penetration profiles associated with delivery of collimated or dispersed fluid jets generated by a Lorentz-force actuated jet injector. Jet injection into polyacrylamide gels, a commonly used tissue analog [26], and porcine abdominal tissue injections was analyzed in real time using high-speed videography and a high-speed X-ray imaging system [47]. The content of this chapter submitted to 37^{th} Annual International Conference of the IEEE Engineering in Medicine and Biology Society (EMBC) [48].

5.1 Experimental Method

Ex vivo porcine abdominal tissue was prepared as described in Section 3.3.1. Tissue to be injected with tissue marking dye (Polysciences Inc.) [?] was cut to fit into clear plastic 80 mm × 65 mm (L×W) × 30 mm (H) containers while tissue to be injected with radiopaque dye was cut to fit into 80 mm × 25 mm (L×W) × 30 mm (H) containers. Gel (10%) was prepared by mixing an appropriate volume of 40% acrylamide stock (Bio-Rad laboratories) [49] with water. Polymerization was initiated by the addition of ammonium persulfate and TEMED and injection into gels was visualized using 0.25% bromophenol blue (Sigma Aldrich) [50].

All injections were performed using Injex 30 ampoules (INJEX Pharma) of which the nozzle orifices were viewed under 20x magnification. Prior to injections into acrylamide gels and post-mortem porcine tissue, the ampoule tip was pressed on to the tissue surface to create the appropriate pre-load, as measured by two load cells (LSB200, Futek). The contact forces applied from the ampoule tip were 1.3 N for the post-mortem porcine tissue and 0.1 N for the acrylamide gel. Porcine tissue samples injected with tissue marking dye were medially sectioned, splayed injection side up, and photographed.

Ejection of fluid from the ampoules and injection of fluid into acrylamide gets were each recorded by a high-speed CMOS video camera (Phantom V9, Vision Research) at a frame rate of 6400 fps with an exposure time of 156 μs and 4300 fps with an exposure time of 232 μs, respectively. Real time imaging of jet injection of radiopaque dye into tissue used high-speed x-ray imaging system with its optimal parameters described in Chapter 3.

5.2 Jet Stream of Commercially Available Ampoules for Jet Injector

Jet shapes of commercially available ampoules for jet injector (Injex Ampoule, INJEX Pharma Ltd.) were investigated by taking high-speed videos of water ejected from the

nozzles. As shown in Fig. 5-1, all the ejections showed sprayed water around a main stream, which possibly indicate that the water was deflected by an obstacle when it was ejected from the nozzle. In addition, the shapes of each jet stream at high jet velocity varied dramatically within tested ampoules. Among eleven ampoules tested, only two ampoules (ampoule 3 and ampoule 4) showed relatively collimated jet shapes determined by water ejection at high velocity. Other jet shapes were dispersed and skewed.

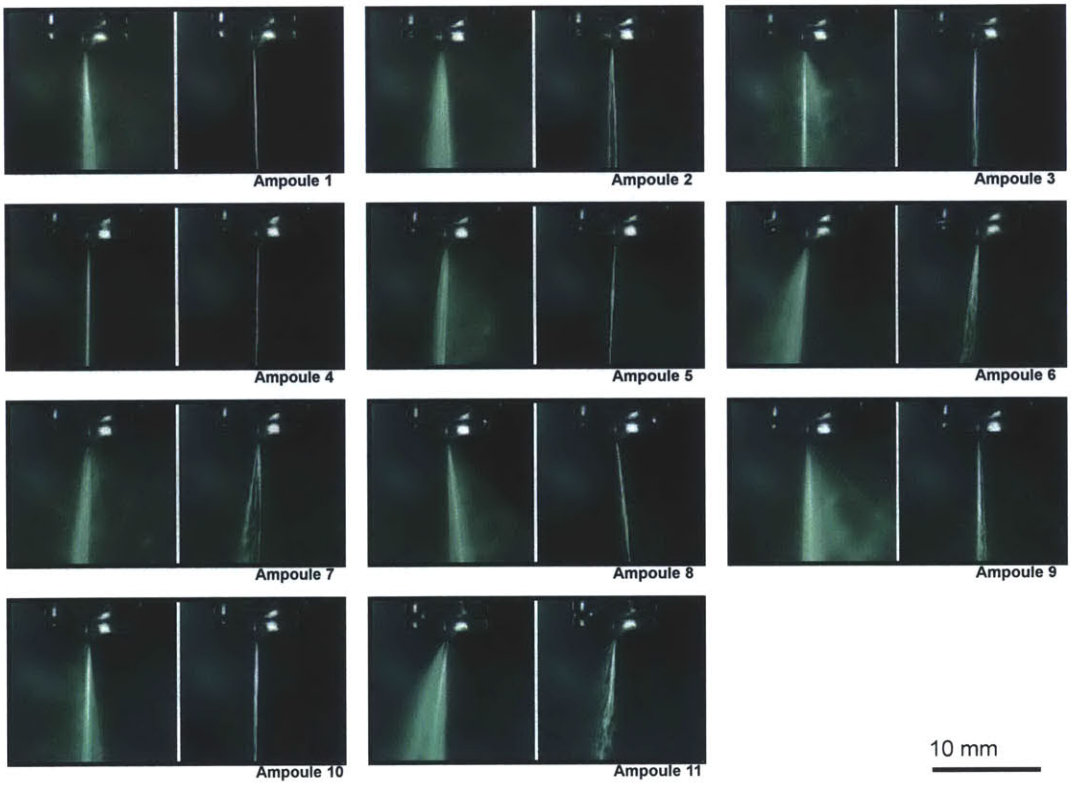

Figure 5-1: Jet shape images of eleven ampoules were captured at two different jet velocities: v_{jet} of 160 m/s (left) and v_{ft} of 50 m/s (right).

Furthermore, the shape of each nozzle and nozzle orifice was viewed under a microscope with 165× magnification to assess irregularities between ampoules (Fig. 5-2). Measured nozzle orifice diameters were found to vary from 170 μm to 270 μm and in most ampoules, the inside edge of the nozzle appeared as a ragged, rather than a smooth line. These irregularities could have influence the reliability and repeatability

of jet injection.

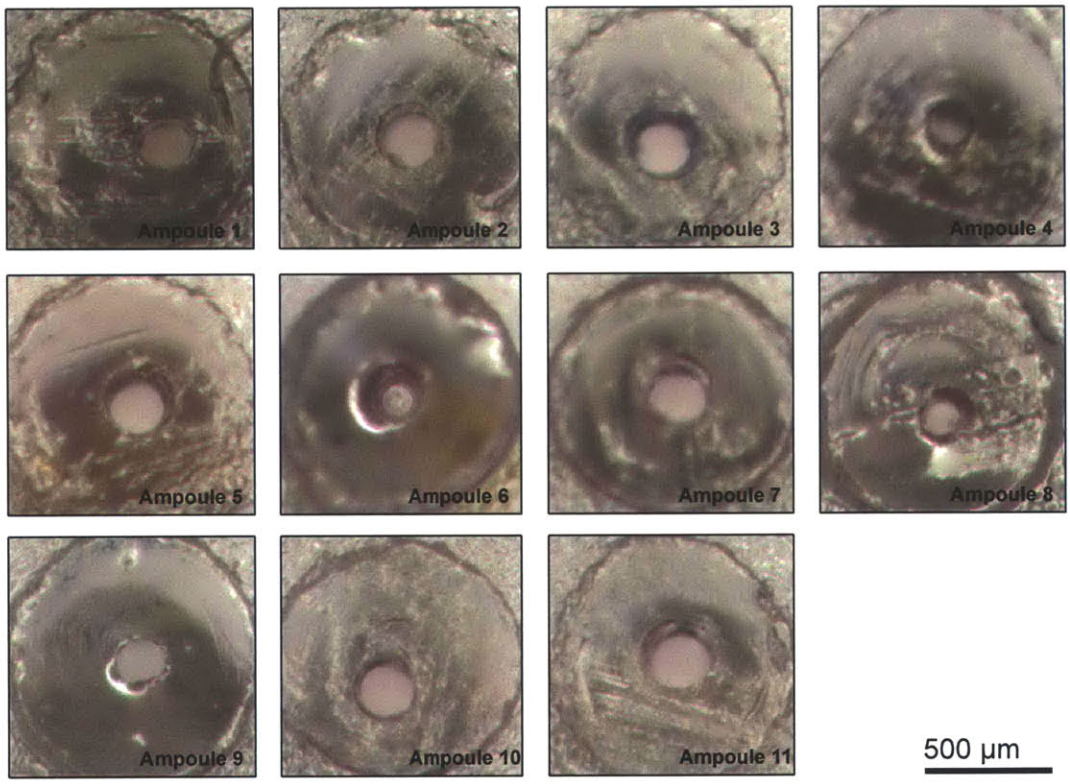

Figure 5-2: Images of nozzle shapes used for water ejection test in Fig. 5-1. Diameters of nozzle ranged from 170 µm (ampoule 8) to 270 µm (ampoule 3).

5.3 Effect of Jet Shape on Jet Dispersion

5.3.1 Jet Stream Representative of a Collimated and Dispersed Shape

Among those ampoules tested, two ampoules with different jet shapes were chosen to evaluate the effect of jet shape on penetration depth and dispersion. The nozzle shape and jet shape of each ampoule at two different jet velocities are shown in Fig. 5-3. The diameters of nozzle for ampoule A and ampoule B are 240 µm and 230 µm, respectively (Fig. 5-3A). While both nozzles were of comparable diameter, fluid

flow from ampoule A was collimated whereas flow from ampoule B (Fig. 5-3B) was dispersed at both jet velocities.

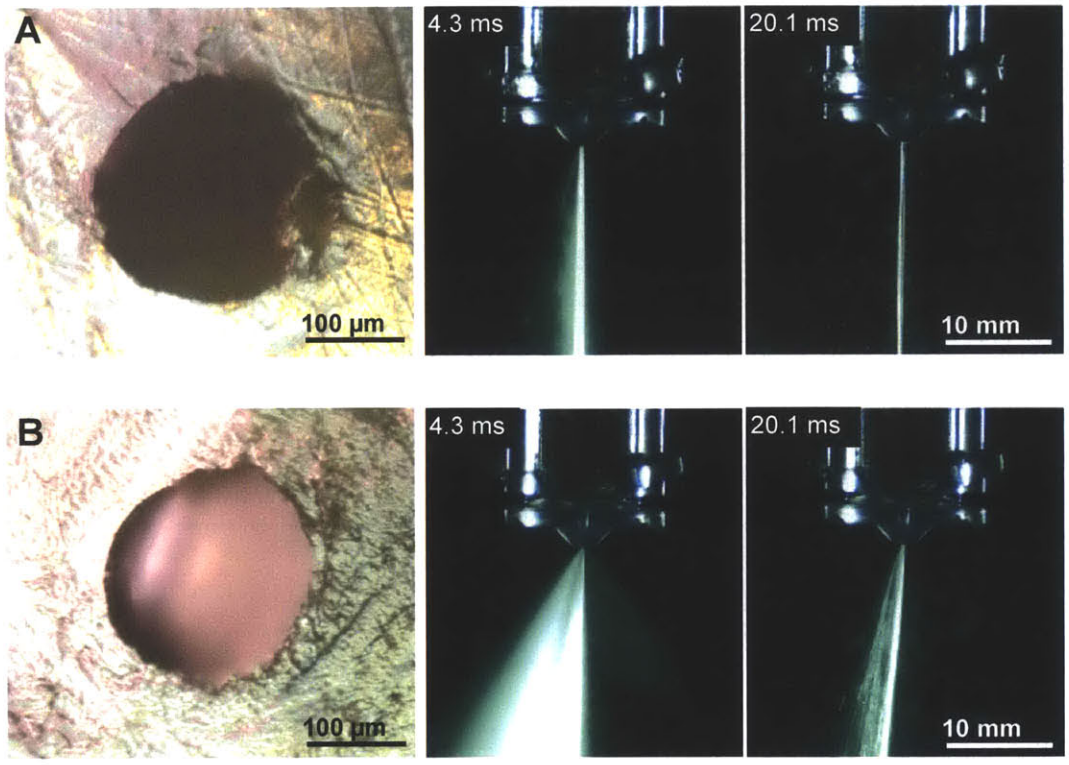

Figure 5-3: Nozzle shape and corresponding jet shape for ampoule A (A) and B (B). Images of jet shape for each ampoule were taken during v_{jet} of 200 m/s (t=4.3 ms) and v_{ft} of 50 m/s (t=20.1 ms).

5.3.2 Jet Injection Profiles

The power of a turbulent jet at the nozzle exit can be expressed in terms of mass flow rate, $\dot{m}$, and exit velocity, u_0, as shown below [51],

$$P_0 = \frac{1}{2}\dot{m}u_0^2. \tag{5.1}$$

The mass flow rate of the fluid, $\dot{m}$, is determined by its geometry, density and exit

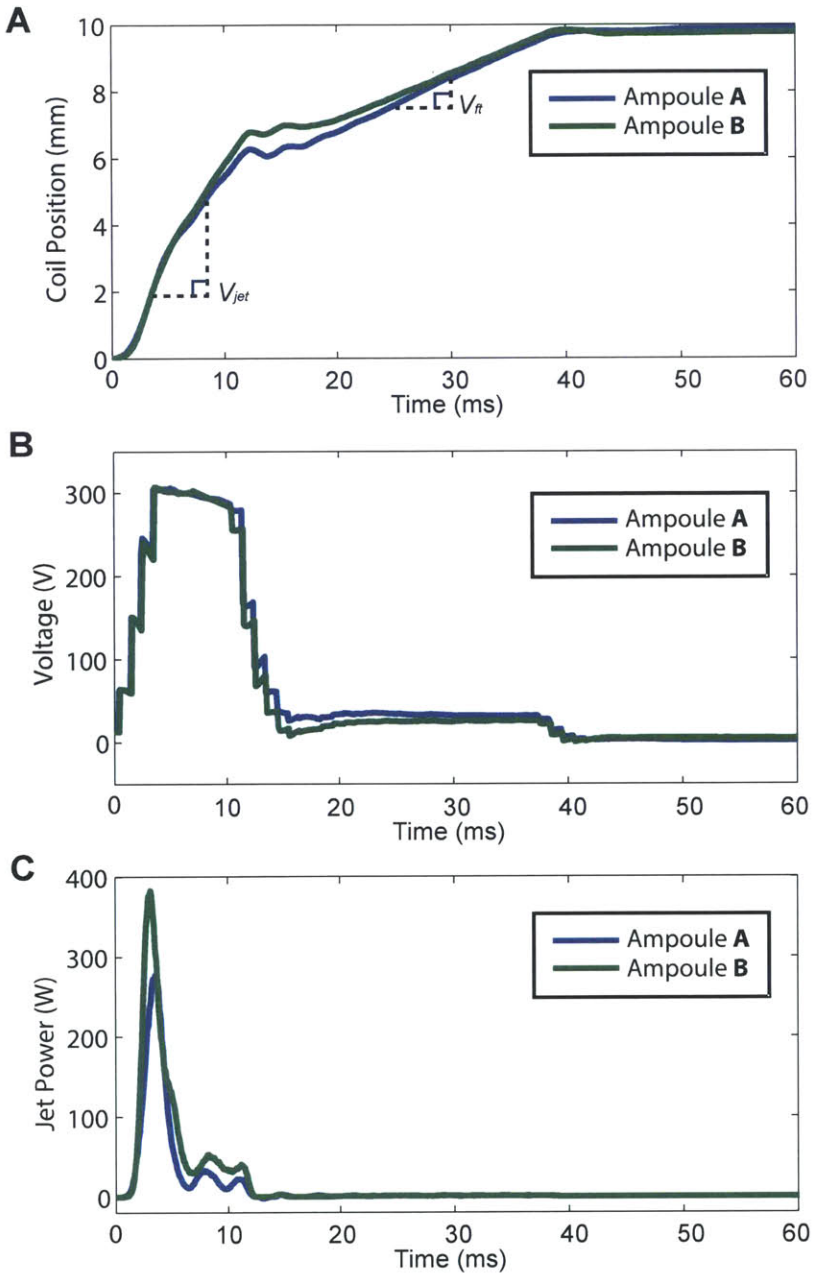

Figure 5-4: Position(A), applied voltage (B) and calculated jet power (C) profiles of ampoule A and ampoule B during tissue injection of 100 μL tissue marking dye. Set parameters: 200 m/s for v_{jet} and 50 m/s for v_{ft} (see Fig. 2-5).

velocity. For a jet with a cylindrical shape it is defined as,

$$\dot{m} = \rho A_0 u_0, \tag{5.2}$$

where ρ is the fluid density and A_0 is the cross-sectional area of the nozzle. Given that A_0 can be expressed in terms of the nozzle diameter, D_0, substituting (5.2) into (5.1) yield,

$$P_0 = \frac{1}{8}\pi\rho D_0^2 u_0^3. \tag{5.3}$$

To calculate the jet power of each ampoule, the average jet velocities of fluid exiting the nozzles of two ampoules were estimated volumetrically from the coil speed as measured from potentiometer and the ratio of the area of the piston and nozzle. While calculating average jet velocity using the actual pressure inside the ampoule will give a better estimation of the jet power, calculating the jet power from the coil velocity provides a reasonable estimation of jet power permitting comparison between ampoules.

Position, applied voltage, and jet power profiles typical of tissue injections of 100 μL of tissue marking dye are shown for ampoules A and B in Fig. 5-4. While the voltage profiles for ampoules A and B are similar between ampoules, the coil positions and jet power profiles differ.

5.3.3 Injection into Tissue Analog

To verify the importance of the jet shape on the fluid dispersion pattern, ampoules A and B were used to inject a consistent volume of fluid at consistent v_{jet}, v_{ft} and t_{jet} into 10% acrylamide gels (see Fig. 5-5). Consistent with earlier studies [19], the high speed fluid jet punctures the gel surface and erodes the matrix to form a channel of which the depth is defined by v_{jet}. Stagnation occurs followed by dispersion of the fluid at a lower jet velocity to form a more bolus like structure. However, as is shown in Fig. 5-5, the depths of penetration of the jet stream for each ampoule

were different; 24.65 ± 2.3 mm for ampoule A and 18.5 ± 0.3 mm for ampoule B. In addition, the point of entry of the jet stream generated by ampoule B and the width of the cavity are greater than that observed for ampoule A; the width of the cavity for B was 4.5 ± 0.1 mm while for ampoule A, it is 2.7 ± 0.2 mm (see Fig. 5-6).

5.3.4 Injection into Tissue

Prior to assessing the effect of jet shape on tissue penetration and dispersion, differential penetration due to variability between tissue samples was evaluated by injection of dye into porcine abdominal tissue harvested from pigs of similar age. A control ampoule presenting a collimated jet stream was used to inject tissue from different animals with a constant volume of dye at a consistent v_{jet}, and v_{ft} (Fig. 5-7). Medially sectioning through the injection sites showed that the jet stream repeatedly penetrated to a comparable depth in all tissue blocks and exhibited similar dispersion patterns; depths of approximately 14.5 ± 1.4 mm were calculated for Fig. 5-7B and 12.8 ± 2.9 mm for Fig. 5-7C. These same blocks when injected with ampoules exhibiting collimated or dispersed jet streams displayed remarkably different penetration depths and dispersion patterns (Fig. 5-8). The collimated jet streams breached the muscle, exhibited a dispersion pattern similar to that observed following injection into acrylamide gels, and reached an average depth of 15.2 ± 1.5 mm (ampoule A). The more dispersed jet stream associated with ampoule B resulted in a more bowl-shaped, shallow subcutaneous injection with an average depth of 3.4 ± 0.6 mm (see Fig. 5-9).

The results from the experiments suggest that the shape of a jet stream can be an important parameter in fluid dispersion into the tissue. Although more investigation is needed to evaluate the fluid dynamics of jet streams of different shapes, the current data provides us some insight. Previous papers note that higher peak and average jet power can lead to deeper penetration of jet injection into porcine skin [18] [21]. However, it is clearly shown that this was not the case if the shapes of the jet streams are different from each other. That is, lower jet power with a collimated jet shape can penetrate porcine tissue more deeply than higher jet power with a dispersed jet

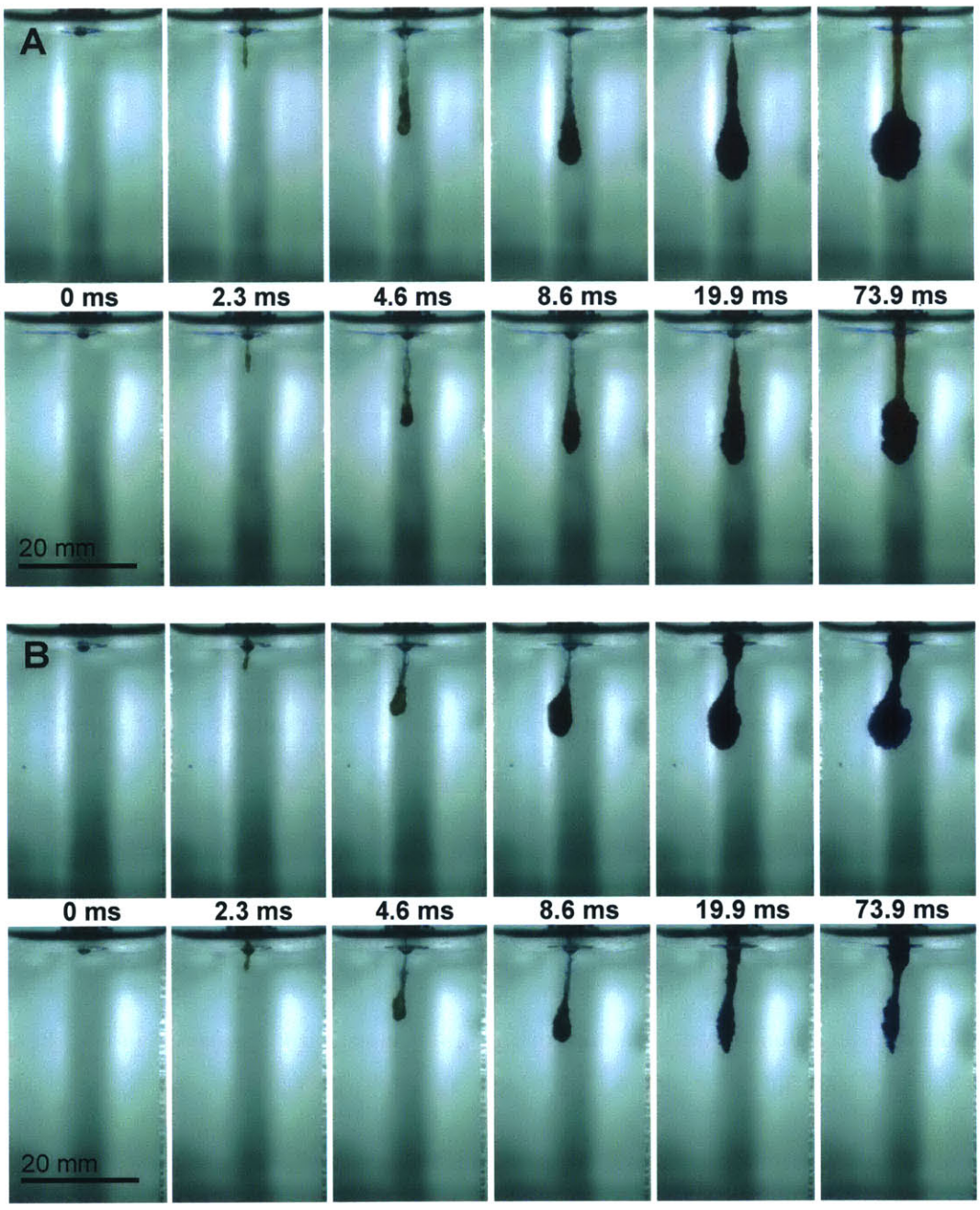

Figure 5-5: Injections into tissue analog (acrylamide gel) with ampoule A (A) and ampoule B (B). Two injections were made for each ampoule. The penetration depth by ampoule A, 24.6 $\pm$ 2.3 mm, was deeper than that by ampoule B, 18.5 $\pm$ 0.3 mm.

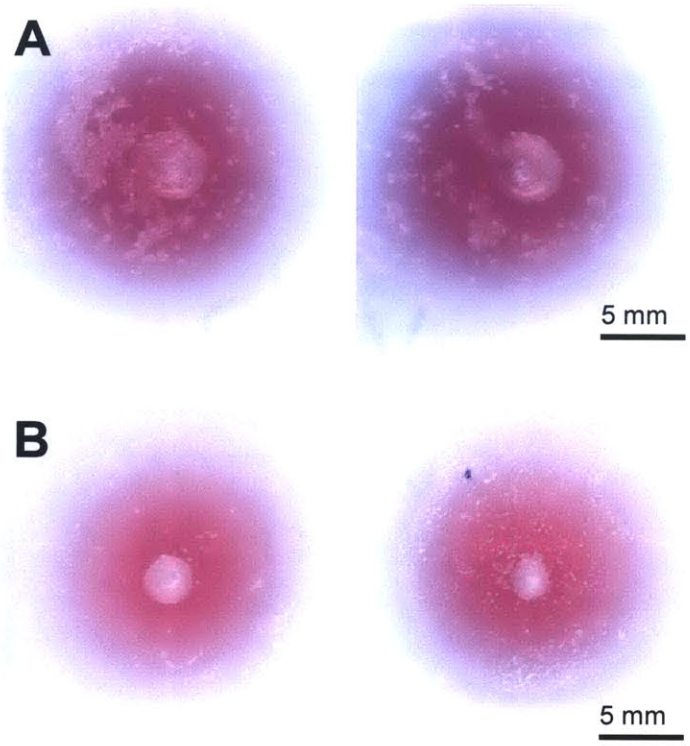

Figure 5-6: The cavities of acrylamide gel created by jet injections with ampoule A (A) and ampoule B (B). The width of the cavity for ampoule B was 2.7 ± 0.2 mm and that for ampoule B was 4.5 ± 0.1 mm.

shape. The velocity of a dispersed jet has both radial and axial components whereas the velocity of a collimated jet has only an axial component as illustrated in Fig. 5-10. Therefore, given two jets of the same total fluid power, the resultant power that is transferred along the direction of injection is smaller for a dispersed jet than that of a collimated jet. This is especially important in jet injection if the injection is designed to be delivered into a specific target layer. In addition, this work underscores that the repeatability of jet injection is highly dependent on the nozzle geometry being uniform across all ampoules.

5.3.5 X-ray Injection

In order to capture the dynamics of the injections associated with different jet streams, injections were imaged in real time using a high-speed X-ray imaging system as shown

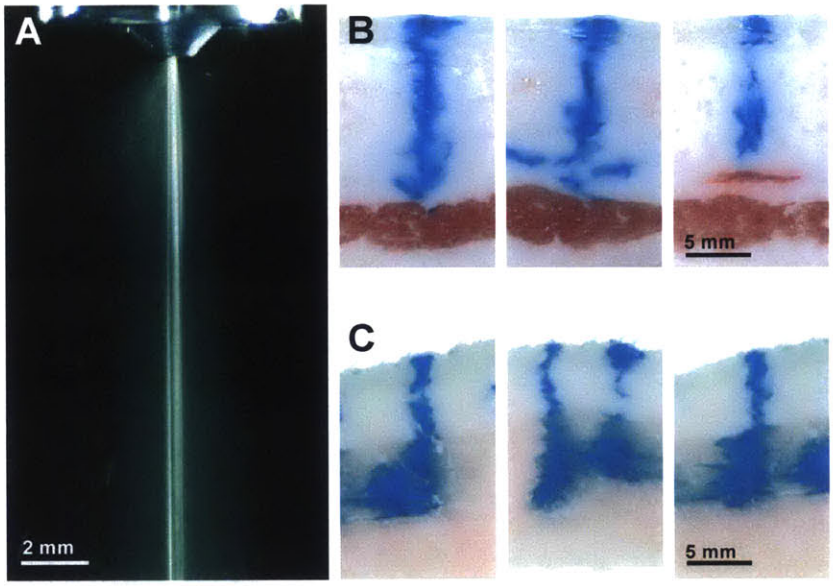

Figure 5-7: Jet shape of ampoule C (A), injection with ampoule C into porcine tissue **block A** (B) and **block B** (C).

in Fig. 5-11. As expected, a small volume of fluid pooled on the surface of the tissue until the pressure was sufficient to breach the stratum corneum. The breaching times for both jets were similar (3 ms $<$ t $<$ 3.5 ms) because at this point both jet streams were collimated. Once the epidermis was breached, the collimated jet penetrated to the muscle at t = 7.5 ms while the dispersed jet was only able to reach the subcutaneous layer at t = 4 ms.

High-speed X-ray imaging of jet injection with different jet shapes suggests that the jet shape can be used as another parameter to control the dispersion pattern. Earlier work using high-speed X-ray imaging demonstrated that the residual volume left on the surface of the tissue is primarily due to collection of fluid prior to the jet reaching a pressure capable of breaching the skin [47]. Since the dispersed jet stream has a fan-like shape with less directed force, it could be assumed that it uses more fluid volume before breaching the surface of issue. However as is shown in Fig. 5-11, the breaching happens at a similar time for both ampoules A and B, which means they uses a similar amount of fluid before breaching the surface. The fluid left on the surface is one of the parameters that determine the efficiency of the jet injection

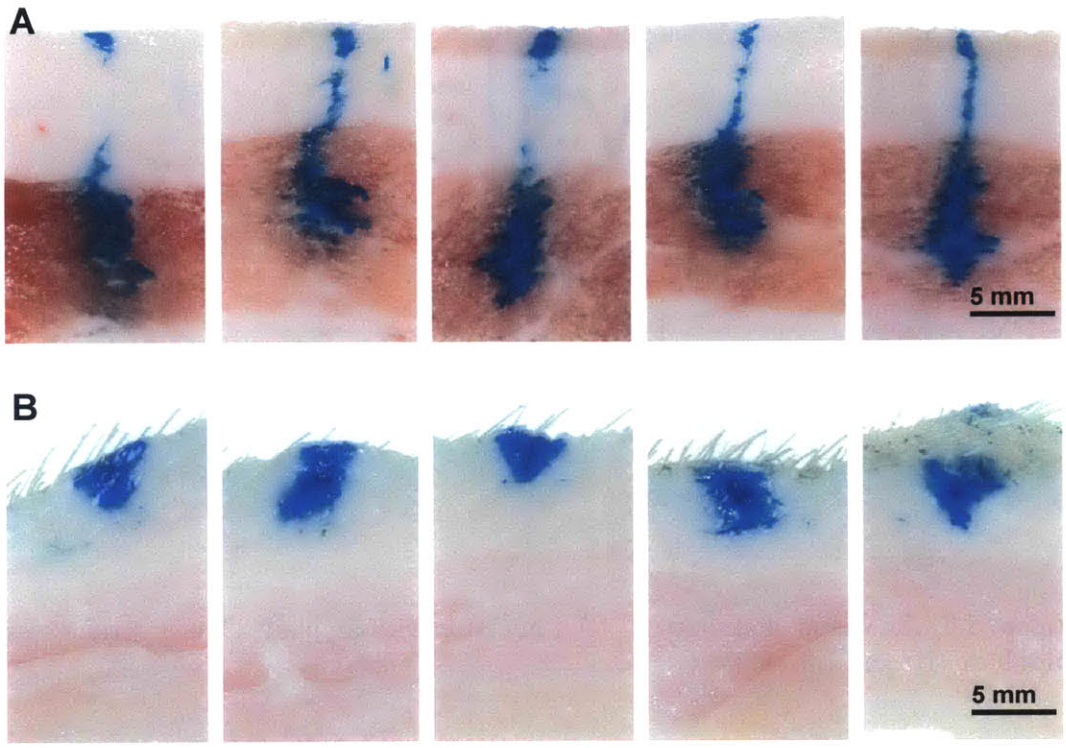

Figure 5-8: Injection into porcine tissue **block A** with ampoule A (A) and tissue **block B** with ampoule B (B).

because it indicates the amount of fluid not injected into skin. Therefore, a dispersed jet stream does not decrease efficiency of injection. In addition, this result opens the possibility of using a dispersed jet shape with adjusted velocity waveform to target a shallow layer of tissue.

5.4 Conlcusion

The effects of jet shape on the dispersion pattern into polyacrylamide gels and *ex vivo* porcine abdominal tissue was explored using a Lorentz-force actuated jet injector. Optimized high-speed X-ray imaging system was used to observe the dynamics of the dispersion mechanism for each injection in real time. It was shown that a collimated jet stream results in greater tissue penetration than a dispersed jet stream.

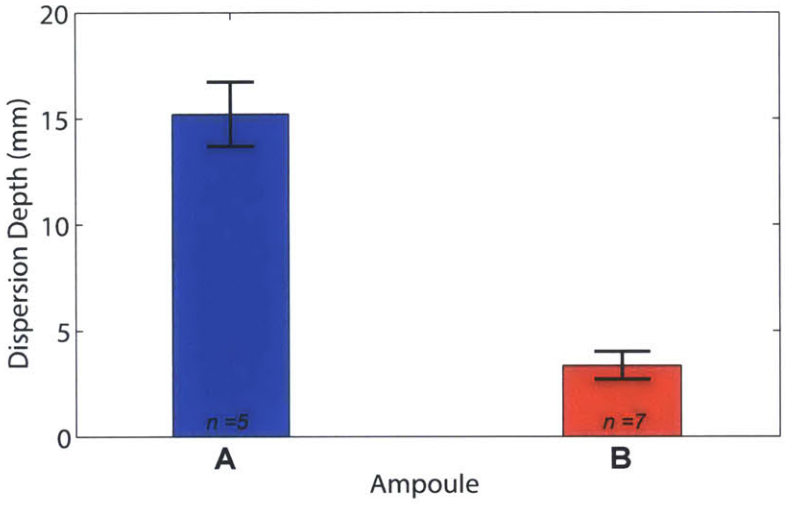

Figure 5-9: The dispersion depths measured for injections with ampoule A and ampoule B. Injection parameters were kept constant as v_{jet} = 200 m/s and v_{ft} = 50 m/s.

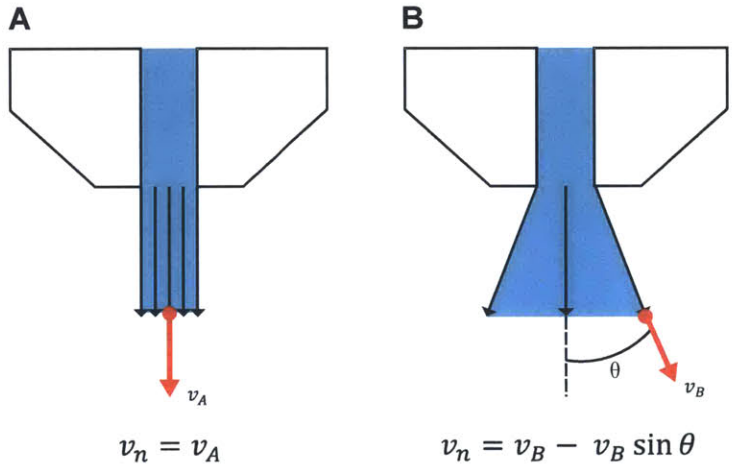

Figure 5-10: Fluid flows of a collimated jet shape (A) and a dispersed jet shape (B) Since the fluid flow of dispersed jet shape has a radial velocity component, the magnitude of the axial velocity for a dispersed jet is smaller than that of a collimated jet, under the assumption that the mass flow rate of both jets are the same.

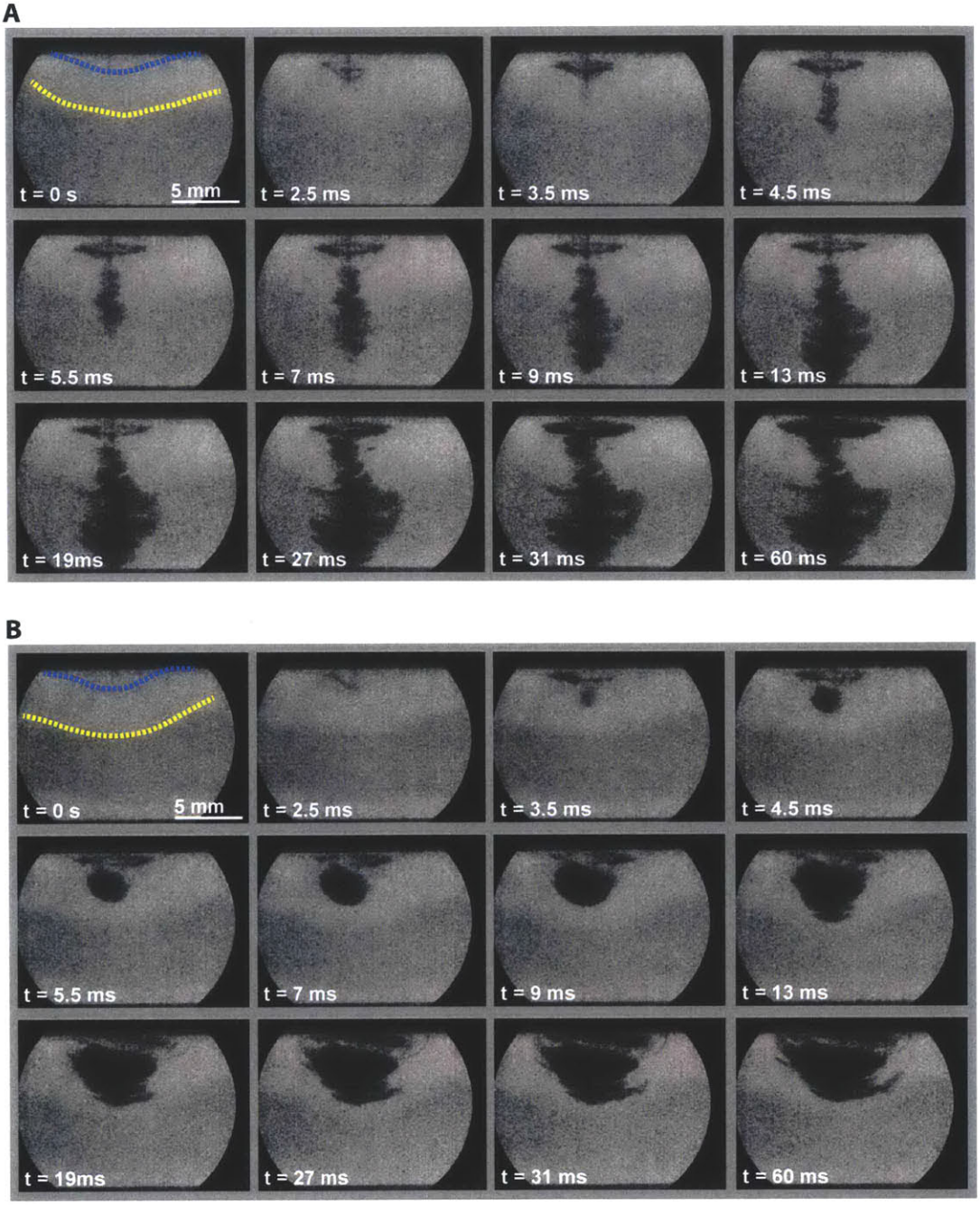

Figure 5-11: Frames from x-ray videos taken of a 100 μL jet injection into porcine tissue with ampoules with two different jet shapes; an ampoule with a collimated jet shape (A) and a dispersed jet shape (B).

Chapter 6

Conclusion

The aim of this work was to explore parameters that have influence on jet injection dynamics. To provide more realistic jet injection experimental result with high enough image quality, the previous high-speed x-ray imaging system was optimized and modified. By using an asymmetric dimension for the porcine tissue, we were able to obtain a reasonable stress distribution and deformation of tissue in jet injection experiment while maintaining the x-ray image quality. High-speed x-ray imaging of jet injections with modified experiment setup were conducted to explore the parameters of jet injection. It was shown that the presence of contact force reduced the critical stress that a jet required to achieve to penetrate the surface of the tissue by providing pre-tension to the tissue. In addition, the effect of the jet shape on the dispersion pattern of a needle free jet injector was investigated. From the results of jet injections into tissue analog and *ex vivo* porcine tissue, it was concluded that a jet with a collimated jet shape can penetrated more deeply than that with a dispersed jet shape.

Furture experimental work following this thesis will include more jet injection experiments with various contact forces and discover quantitative relationship between the contact force and the critical stress. Furthermore, an experiment using a hand-held needle-free jet injection device, along with appropriate measurement for the contact force, will further understanding on how the contact force affects the *in vivo* tissue injection. Designing and manufacturing different nozzle geometries which

can generate different types of jet shapes will allow us to use the jet shape as an important parameter which can determine the jet dispersion pattern.

Bibliography

[1] Occupational Safery Health administration (OSHA). Needlestick/Sharp Injuries. `https://www.osha.gov/SLTC/etools/hospital/hazards/sharps/sharps.html`, Web.10 May 2015.

[2] L. Simonsen, A. Kane, J. Lloyd, M. Zaffran, and M. Kane. Unsafe injections in the developing world and transmission of bloodborne pathogens: a review. *Bulletin of the World Health Organization*, 77(10):789–800, 1999.

[3] S. Mitragotri. Immunization without needles. *Nature Reviews Immunology*, 5(12):905–916, December 2005.

[4] R. A. Hingson and J. G. Hughes. Clinical studies with jet injection; a new method of drug administration. *Current Researches in Anesthesia & Analgesia*, 26(6):221–230, December 1947.

[5] Injex Pharma Ltd. Miami, FL. `http://www.injex.com`.

[6] PharmaJet. Golden, CO. `http://www.pharmajet.com`.

[7] Bioject Medical Techonologies. Lake Forest, CA. `http://www.bioject.com`.

[8] Inc. Valeritas. Bridgewater, NJ. `http://www.valeritas.com`.

[9] N. Inoue, H. Todo, D. Iidaka, Y. Tokudome, F. Hashimoto, T. Kishino, and K. Sugibayashi. Possibility and effectiveness of drug delivery to skin by needle-free injector. *International Journal of Pharmaceutics*, 391(1-2):65–72, May 2010.

[10] W. Walther, U. Stein, I. Fichtner, and P. M. Schlag. Low-volume jet injection for efficient nonviral in vivo gene transfer. *Molecular Biotechnology*, 28(2):121–128, October 2004.

[11] S. Mitragotri. Current status and future prospects of needle-free liquid jet injectors. *Nature Reviews. Drug Discovery*, 5(7):543–548, July 2006.

[12] R. Wang, J. Epstein, F. M. Baraceros, E. J. Gorak, Y. Charoenvit, D. J. Carucci, R. C. Hedstrom, N. Rahardjo, T. Gay, P. Hobart, R. Stout, T. R. Jones, T. L. Richie, S. E. Parker, D. L. Doolan, J. Norman, and S. L. Hoffman. Induction of CD4(+) T cell-dependent CD8(+) type 1 responses in humans by a malaria DNA vaccine. *Proceedings of the National Academy of Sciences of the United States of America*, 98(19):10817–10822, September 2001.

[13] J. Williams, L. Fox-Leyva, C. Christensen, D. Fisher, E. Schlicting, M. Snowball, S. Negus, J. Mayers, R. Koller, and R. Stout. Hepatitis A vaccine administration: comparison between jet-injector and needle injection. *Vaccine*, 18(18):1939–1943, March 2000.

[14] I. Parent du Châtelet, J. Lang, M. Schlumberger, E. Vidor, G. Soula, A. Genet, S. M. Standaert, and P. Saliou. Clinical immunogenicity and tolerance studies of liquid vaccines delivered by jet-injector and a new single-use cartridge (Imule): comparison with standard syringe injection. Imule Investigators Group. *Vaccine*, 15(4):449–458, March 1997.

[15] A. M. Weintraub and M. P. Ponce de Leon. Potential for cross-contamination from use of a needleless injector. *American Journal of Infection Control*, 26(4):442–445, August 1998.

[16] G. Wijsmuller and D. E. Snider. Skin testing: a comparison of the jet injector with the Mantoux method. *The American Review of Respiratory Disease*, 112(6):789–798, December 1975.

[17] R. Worth, J. Anderson, R. Taylor, and K. G. Alberti. Jet injection of insulin: comparison with conventional injection by syringe and needle. *BMJ*, 281(6242):713–714, September 1980.

[18] J. Schramm and S. Mitragotri. Transdermal Drug Delivery by Jet Injectors: Energetics of Jet Formation and Penetration. *Pharmaceutical Research*, 19(11):1673–1679, November 2002.

[19] K. Comley and N. Fleck. Deep penetration and liquid injection into adipose tissue. *Journal of Mechanics of Materials and Structures*, 6(1-4):127–140, June 2011.

[20] O. A. Shergold, N. A. Fleck, and T. S. King. The penetration of a soft solid by a liquid jet, with application to the administration of a needle-free injection. *Journal of Biomechanics*, 39(14):2593–2602, 2006.

[21] J. Schramm-Baxter and S. Mitragotri. Needle-free jet injections: dependence of jet penetration and dispersion in the skin on jet power. *Journal of Controlled Release*, 97(3):527–535, July 2004.

[22] J. Baxter and S. Mitragotri. Jet-induced skin puncture and its impact on needle-free jet injections: experimental studies and a predictive model. *Journal of Controlled Release: Official Journal of the Controlled Release Society*, 106(3):361–373, September 2005.

[23] A. J. Taberner, N. B. Ball, N. C. Hogan, and I. W. Hunter. A portable needle-free jet injector based on a custom high power-density voice-coil actuator. *Conference proceedings: ... Annual International Conference of the IEEE Engineering in Medicine and Biology Society. IEEE Engineering in Medicine and Biology Society. Annual Conference*, 1:5001–5004, 2006.

[24] D. M. Wendell, B. D. Hemond, N. C. Hogan, A. J. Taberner, and I. W. Hunter. The effect of jet parameters on jet injection. *Conference proceedings: ... Annual International Conference of the IEEE Engineering in Medicine and Biology Society. IEEE Engineering in Medicine and Biology Society. Annual Conference*, 1:5005–5008, 2006.

[25] N. C.e Hogan, B. D. Hemond, D. M. Wendell, A. J. Taberner, and I. W. Hunter. Delivery of active collagenase to skin using a lorentz-force actuated needle-free injector. *Conference proceedings: ... Annual International Conference of the IEEE Engineering in Medicine and Biology Society. IEEE Engineering in Medicine and Biology Society. Annual Conference*, 1:5611–5616, 2006.

[26] B. D. Hemond, A. Taberner, C. Hogan, B. Crane, and I. W. Hunter. Development and Performance of a Controllable Autoloading Needle-Free Jet Injector. *Journal of Medical Devices*, 5(1):015001–015001, February 2011.

[27] Mouser Electronics. Mansfield, TX. `www.mouser.com`.

[28] J. H. Chang. *Needle-free interstitial fluid acquisition using a Lorentz-force actuated jet injector.* Thesis, Massachusetts Institute of Technology, 2014.

[29] National Instruments. Austin, TX. `www.ni.com`.

[30] A. Taberner, N. C. Hogan, and I. W. Hunter. Needle-free jet injection using real-time controlled linear Lorentz-force actuators. *Medical Engineering & Physics*, 34(9):1228–1235, November 2012.

[31] Anatomy of skin. National Cancer Institue . `http://training.seer.cancer.gov/melanoma/anatomy/`, Web.10 May 2015.

[32] C. H. Daly. Biomechanical properties of dermis. *The Journal of Investigative Dermatology*, 79 Suppl 1:17s–20s, July 1982.

[33] Phsics of the x-ray tube. wikiradiography. `http://www.wikiradiography.net/page/Physics+of+the+X-Ray+Tube`, Web. 10 May 2015.

[34] Production of X-rays. Radiation Therapy Technology School. `http://www.tc.umn.edu/~watan016/Teaching.htm`, Web. 10 May 2015.

[35] Production of X-rays. NDT Resource Cnter. `http://www.tc.umn.edu/~watan016/Teaching.htm`, Web.10 May 2015.

[36] J. Schramm-Baxter, J. Katrencik, and S. Mitragotri. Jet injection into polyacrylamide gels: investigation of jet injection mechanics. *Journal of Biomechanics*, 37(8):1181–1188, August 2004.

[37] Hamamatsu. Bridgewater, NY. `www.sourceray.com`.

[38] Photek Limited. East Sussex, UK. `www.photek.com`.

[39] T. P. Sullivan, W. H. Eaglstein, S. C. Davis, and P. Mertz. The pig as a model for human wound healing. *Wound Repair and Regeneration: Official Publication of the Wound Healing Society [and] the European Tissue Repair Society*, 9(2):66–76, April 2001.

[40] J. L. Prince and J. Links. *Medical Imaging Signals and Systems.* Prentice Hall, Boston, 2 edition edition, March 2014.

[41] The National Institute of Standards and Technology (NIST). X-Ray Mass Attenuation Coefficients. `https://http://physics.nist.gov/PhysRefData/XrayMassCoef/tab4.html`, Web.10 May 2015.

[42] Inc. The MathWorks. Natic, MA. `www.mathworks.com`.

[43] Futek. Irvine, CA. `www.futek.com`.

[44] J. Ankersen, A. E. Birkbeck, R. D. Thomson, and P. Vanezis. Puncture resistance and tensile strength of skin simulants. *Proceedings of the Institution of Mechanical Engineers. Part H, Journal of Engineering in Medicine*, 213(6):493–501, 1999.

[45] Nanoprobes. Yaphank, NY. `www.nanoprobes.com`.

[46] R. M. J. Williams, N. C. Hogan, P. M. F. Nielsen, I. W. Hunter, and A. J. Taberner. A computational model of a controllable needle-free jet injector. *Conference proceedings: ... Annual International Conference of the IEEE Engineering in Medicine and Biology Society. IEEE Engineering in Medicine and Biology Society. Annual Conference*, 2012:2052–2055, 2012.

[47] J. H. Chang, N.C. Hogan, and I. W. Hunter. High-speed X-ray imaging of needle-free jet injections. In *2014 IEEE 11th International Symposium on Biomedical Imaging (ISBI)*, pages 473–476, April 2014.

[48] 37$^{\text{th}}$ Annual International Conference of the IEEE Engineering in Medicine and Biology Society (EMBC). Milano, Italy. `embc.embs.org/2015/`.

[49] Bio-Rad Laboratories. Hercules, CA.

[50] Sigma-Aldrich. St. Louis, MO.

[51] P. J. Pritchard. *Fox and McDonald's Introduction to Fluid Mechanics.* Wiley, Hoboken, NJ : Chichester, 8 edition edition, October 2011.